(2)

UNCLASSIFIED

SECURITY CLASSIFICATION OF THIS PAGE

DTIC ELECTE MAY 30 1990 B C8 D

AD-A222 044

REPORT DOCUMENTATION PAGE

1a. REPORT SECURITY CLASSIFICATION: UNCLASSIFIED	1b. RESTRICTIVE MARKINGS
2a. SECURITY CLASSIFICATION AUTHORITY	3. DISTRIBUTION/AVAILABILITY OF REPORT: Approved for public release; distribution unlimited
SCHEDULE	
T NUMBER(S)	5. MONITORING ORGANIZATION REPORT NUMBER(S): AFOSR-TR- 90-0544
6a. NAME OF PERFORMING ORGANIZATION: SRI International	6b. OFFICE SYMBOL (if applicable): 634
7a. NAME OF MONITORING ORGANIZATION: Air Force Office of Scientific Research USAF, AFOSR	
6c. ADDRESS (City, State, and ZIP Code): 333 Ravenswood Ave. Menlo Park, CA 94025	7b. ADDRESS (City, State, and ZIP Code): Bldg. 410 Bolling AFB, D.C. 20332-6448
8a. NAME OF FUNDING/SPONSORING ORGANIZATION: Air Force Office of Scientific Research	8b. OFFICE SYMBOL (if applicable): AFOSR/NP
9. PROCUREMENT INSTRUMENT IDENTIFICATION NUMBER: F49620-85-K-0013	
8c. ADDRESS (City, State, and ZIP Code): Bldg. 410 Bolling AFB, D.C. 20332-6448	10. SOURCE OF FUNDING NUMBERS: PROGRAM ELEMENT NO. 61102F; PROJECT NO. 2301; TASK NO. A8; WORK UNIT ACCESSION NO.

11. TITLE (Include Security Classification)

PLASMA CLOAKING: AIR CHEMISTRY, BROADBAND ABSORPTION, AND PLASMA GENERATION

12. PERSONAL AUTHOR(S)

Robert J. Vidmar

13a. TYPE OF REPORT	13b. TIME COVERED	14. DATE OF REPORT (Year, Month, Day)	15. PAGE COUNT
Final	FROM 5/15/85 TO 12/14/90	1990 February	112

16. SUPPLEMENTARY NOTATION

SRI Project 8656

17. COSATI CODES		
FIELD	GROUP	SUB-GROUP
20	09	
17	04	

18. SUBJECT TERMS (Continue on reverse if necessary and identify by block number)

Atmospheric plasma, broadband absorber, cloaking device, Epstein profile, noble gases, plasma generation. ~~RAM~~ EES

19. ABSTRACT (Continue on reverse if necessary and identify by block number)

Plasmas with electron number densities from 10^9 cm^{-3} to 5×10^{11} cm^{-3} generated in air or a noble gas constitute tenuous plasmas. If the ambient pressure is near atmospheric, so that the gas density is of the order of 10^{16} cm^{-3} to 10^{19} cm^{-3}, then the plasma is collisional, and the cold collisional dispersion relation predicts electromagnetic characteristics. A plasma generated by an electron beam or by photoionization produces a spatially decreasing electron density. This spatial electron density, approximated ac an Epstein profile, results in low backscatter and high attenuation. Bandwidth and attenuation are quantified. An air–chemistry deionization solution is described that estimates plasma lifetime. The lifetime and electron density are sufficient to estimate the power required by a plasma absorber. Plasmas generated in air require a high input power. A plasma generated in a noble gas, seeded with a readily ionized material, and confined by a membrane, requires much less power, and is technically feasible. Plasma absorber would exceed the capabilities of carbon–based absorber by 40 dB and is broadband from VHF through X–band. This plasma can be used as a switchable cloaking device to replace carbon–based absorber.

20. DISTRIBUTION/AVAILABILITY OF ABSTRACT	21. ABSTRACT SECURITY CLASSIFICATION
☒ UNCLASSIFIED/UNLIMITED ☒ SAME AS RPT ☐ DTIC USERS	UNCLASSIFIED

22a. NAME OF RESPONSIBLE INDIVIDUAL	22b. TELEPHONE (Include Area Code)	22c. OFFICE SYMBOL
Dr. Robert Barker	(202) 767-5011	AFOSR/NP

DD FORM 1473, 84 MAR — 83 APR edition may be used until exhausted. All other editions are obsolete.

SECURITY CLASSIFICATION OF THIS PAGE

UNCLASSIFIED

SRI International

Final Report • February 1990

PLASMA CLOAKING: AIR CHEMISTRY, BROADBAND ABSORPTION, AND PLASMA GENERATION

Robert J. Vidmar, *Senior Research Physicist*
Remote Measurements Laboratory

Prepared for:

Air Force Office of Scientific Research
Directorate of Physical and Geophysical Sciences
AFOSR/NP, Building 410
Boiling AFB, Washington, D.C. 20332-6448

Contract F49620-85-K-0013

SRI Project 8656

Approved by:

TAYLOR W. WASHBURN, *Director*
Remote Measurements Laboratory

JOSEPH J. EASH, *Vice President*
System Technology Division

333 Ravenswood Avenue • Menlo Park, CA 94025-3493 • (415) 326-6200 • FAX: (415) 326-5512 • Telex: 334486

CONTENTS

TABLES

I INTRODUCTION

This report summarizes the results of a three-year investigation conducted by SRI International on the generation and reflective/absorptive properties of man-made atmospheric pressure plasma. The initial thrust was to understand plasma generation in the earth's atmosphere from sea level to 300,000 ft. SRI thus investigated plasma lifetime; or more exactly the deionization solution for a tenuous plasma. That investigation resulted in an air chemistry code specifically set up for the earth's atmosphere and later extended to noble gases [1,2].* Most significantly SRI derived an estimate of plasma lifetime as a function of gas composition, pressure, and electron number density. Lifetime is important because the power required to sustain a man-made tenuous is inversely proportional to lifetime. If the lifetime is long enough the the power required is low and plasma generation becomes feasible.

Motivation for this research was twofold. Man-made plasma in the earth's atmosphere could be used to (1) reflect electromagnetic waves, i.e., an artificial ionospheric mirror [3,4], or (2) absorb electromagnetic waves [5–7]. The cold collisional plasma model [8,9] and theory for reflection from an Epstein profile [10–13] provided a tractable and computationally feasible model for estimating electromagnetic effects. Estimates of the reflection coefficient at 270,000 ft [14; copy attached] quantified the importance of a sharp transition from free space to plasma for the ionospheric mirror application.

The power reflection coefficient for backscatter from a plasma was computed and found to be significantly lower than that for commercially available absorber [15]. The concept of a cloaking device, i.e., a means to reduce electromagnetic backscatter, using a collisional plasma has a relevancy to radar cross section (RCS) measurements and signature control [16,17]. A plasma absorber would operate near the ambient atmospheric pressure (760 torr), be broadband from VHF through X-band, and have a greater theoretical absorption coefficient than any commercially produced carbon-based absorber.

---

* References appear at the end of this report.

An important part of this cloaking concept is estimating the power required to generate a plasma gradient. The basic science that affects the practicality of a cloaking device includes (1) an efficient means of ionization, which determines the energy required to ionize a plasma, and (2) the deionization solution based on gas kinetics, which determines plasma lifetime and power.

The major thrust of this research has been to establish a model for deionization in air and noble gas plasmas. Minimization of the power required to sustain a plasma is directly related to the gas kinetics; specifically, the momentum–transfer collision rate [18] and the deionization time constant for the specific gas mixture used. The air chemistry code developed as a central part of this research quantifies the plasma lifetime in air and in noble gases with trace impurities of air. The net result has been the identification of helium, neon, and argon with impurities kept below 100 ppm as a good (but not minimum) gas mixture for generating a cloaking–device plasma. When that research was nearly complete, attention was focused on practical means of ionization.

Initial interest was on an electron–beam source with an energy of 100 to 300 keV, which could generate the required plasma through the mechanism of impact ionization. Although such a scheme works, has a high input–to–output efficiency, and has been verified experimentally by other researchers, it has some shortcomings. A high–energy electron–beam source is heavy and bulky, has a low duty ratio, and produces X–ray emissions [19].

As an alternative, SRI has identified a simple, safe, compact means of ionization. It is based on ultraviolet (UV) photoionization of an organic vapor and a confinement membrane that is both electrically transparent and chemically compatible with the organic vapor. This ionization method and confinement membrane complete a system for generating a cloaking–device plasma that is inexpensive to construct and suitable for experimental validation studies.

Summary descriptions of the technical issues associated with air chemistry, broadband absorption, and plasma generation are provided in this report, along with supporting documentation.

II TECHNICAL ISSUES

This investigation has spanned nearly five years. Work on theory for reflections and broadband absorption was completed last year. The air chemistry code was completed this year, as was the investigation of an organic vapor suitable for photoionization and a confinement membrane.

A. Air Chemistry

The predictions of plasma lifetime in air and in noble gases with impurities build on an existing data base [20–25]. The range of electron densities investigated was chosen to span the applications of an artificial ionospheric mirror and a cloaking device. Identification of the limiting processes in practical noble gas plasmas [14] provides a theoretical model for prediction of attenuation and attenuation bandwidth as a function of noble gas species and applied power.

1. Additional Reactions. The previously reported 263 chemical reactions among 43 gas species [2] have been increased to 340 reactions among 44 species. The addition of $He(^3S_1)$ provides a better model for a helium plasma. The additional two– and three–body reactions provide model He and $He(^3S_1)$ reactions in plasmas in which their number densities are appreciable. The new reactions (A123–134, B60–75, C26–33, D27–29, and F32–62) are included in Appendix A, which is a complete tabulation of the reactions in the air chemistry code. These reactions permit modeling of plasmas in which helium is the dominant species and air is an impurity. The air chemistry code can (1) model the composition of the earth's atmosphere from sea level to an altitude of 300,000 ft, or (2) model a helium plasma with air as an impurity.

2. Plasma Lifetime. The air chemistry program has been run to determine the 1/e lifetime of a plasma in the earth's atmosphere as a function of both electron number density and altitude. A plot of these data is in Reference 14 (copy attached). A complete listing appears in Appendix B, which is a database for validating the air chemistry code on a new machine.

3. Source Code. An air chemistry code was developed on an IBM AT computer equipped with a math coprocessor chip. A copy of the source code is attached, and the code is briefly described in Appendix C.

B. Broadband Absorption

The prior research on plasma absorption and backscatter from plasma gradients [10–12] provided a solid theoretical base. The theoretical model of a cold collisional plasma [8,9] is sufficient to predict electromagnetic effects of tenuous atmospheric plasmas. The predictions of absorption and reflection based on an Epstein profile provide an estimate of electrical characteristics.

1. Exact Modeling. The value of the Epstein profile gradient scale factor to use for electron beam impact ionization or photoionization is approximate. The method suggested is to plot the anticipated electron distribution and fit an Epstein profile to it. Clearly, this approximate method should be improved by analytically or numerically computing electrical absorption and scattering for the exact electron number density distribution. Modeling the electrical characteristics is tractable. Knowing the exact distribution is a tough problem, because it requires knowing the air chemistry.

For example, a plasma generated in helium by a photoionization pulse has a $1/r^2$ distribution and will deionize at a rate that depends on the electron concentration. The data in Appendix B for a helium plasma with an electron concentration suitable for a cloaking device (10^9 cm^{-3} to 5×10^{11} cm^{-3}) indicate that the plasma lifetime is a function of electron number density. Consequently, the high–electron–density portion of the initial $1/r^2$ distribution decreases in density more quickly than the tail. And, the Epstein profile gradient scale factor flattens out (becomes larger) as a function of time. Clearly, the response of a long electromagnetic pulse will, in turn, become time-dependent.

2. Bandwidth. The Epstein profile gradient scale factor [14] determines the low–frequency limit, and the electron momentum–transfer collision rate determines the high–frequency limit. The low–frequency cutoff is inversely proportional to the plasma gradient scale factor. A plasma that varies from a density of n_0 to $n_0/10$ in a distance of 2 m has a low–frequency cutoff of 150 MHz. Lower or higher cutoff frequencies can be set by altering the means of ionization to produce the required scale factor.

Helium at atmospheric pressure (14.7 psi) has a momentum–transfer collision rate of 253 × 10^9 s^{-1} [18], which produces a high–frequency cutoff of 20 GHz. Argon and neon have a momentum–transfer collision rate that is an order of magnitude lower and so yields a 2–GHz cutoff.

For a space–based cloaking device to have an appreciable high–frequency cutoff, it must have a confinement membrane capable of containing an internal pressure of a few psi. An internal pressure of 14.7 psi of helium would have a high–frequency cutoff of 20 GHz, but 14.7 psi will rupture a thin membrane several meters in diameter [26]. By reducing the internal pressure by a factor of 20 to 0.75 psi, a high–frequency bandwidth of 1 GHz could be realized. Consequently, the thin–shell confinement vessel described by Watters and Vidmar [26, copy attached] would be suitable for space experimentation at frequencies below 1 GHz.

C. Plasma Generation

Two means of ionization, among numerous promising techniques, have been investigated in detail. High–energy electron beam impact ionization and photoionization were investigated because both can readily generate a plasma with a gradient from a single source. A suitable membrane material to confine the plasma without introducing impurities or acting as an electromagnetic scatterer is also necessary. Significant results on these aspects of plasma generation follow.

1. Impact Ionization. Electron impact ionization is a well–developed means of generating a plasma in a gas. The production rates for ionization products and metastables in air due to electron bombardment are known. A production rate table that approximates the generation of ionization by–products has been incorporated in subroutine XRAY (in AIR1.FOR). Metastable species and other ionization by–products are important in modeling conductivity in the late afterglow of an impulsively generated plasma.

As a practical means of powering a cloaking device, impact ionization is an efficient process. But, it has some detracting features. First, the electron must have an energy over 100 keV to penetrate a meter or so into a gas. This potential is sufficient to generate X–rays [19] that constitute (or are perceived by cautious individuals to constitute) an unacceptable health risk.

Second, a small, lightweight, inexpensive, high-repetition-rate X-ray source is not commercially available. A CW source is more desirable but has profound transmission window heating problems that limits the time of CW operation. Thus, a simpler ionization technique was investigated as described below.

2. Photoionization. UV photon sources, 4 -- 400 nm, are commercially available [27], and 10% efficiency at 172 nm (7.22 eV) is possible [28]. Consequently, a substance with an ionization potential up to 6 eV could be ionized with a UV flash lamp using a quartz or magnesium fluoride transmission window. Anderson [29] found that the organic molecule tetrakis(dimethylamino)ethylene (TMAE) is one of many substances that can be used as a seed gas for photoionization with a UV flash lamp.

Rewick et al. [30] have investigated the material compatibility of TMAE with common plastics and found that Kapton, Mylar, and polyethylene can be used to contain TMAE vapor. The vapor pressure and cross section for photoionization of TMAE [29,31] are sufficient for generating plasma with dimensions from a few centimeters to many meters. Electromagnetic validation measurements could be conducted using this means of ionization if a suitable confinement membrane could be constructed.

3. Confinement Membrane. Two common materials, Kapton and Mylar, are candidates for the confinement membrane for a cloaking device. Kapton and Mylar have high tensile strength and a low dielectric constant, which makes their backscatter reflection coefficients low. Watters and Vidmar [26] demonstrated that 2-mil Mylar can be used as a stressed-skin conical structure (32-in. diameter, 96-in. height, 0.75-psi relative pressure) to support targets and antennas during electrical measurements. This structure is ideal for plasma-absorber containment because of its low backscatter and 1-m^3 volume.

For a cloaking device, a 0.25-mil membrane of Kapton or Mylar is adequate for an internal pressure of 0.1 psi. Polyethylene would have to be 2-mil thick and would increase backscatter from the skin by 18 dB compared with Mylar. A thin Mylar membrane becomes an inconsequential electromagnetic scatterer below S-band, where 80 dB of plasma absorption is predicted before reflections from the confinement membrane or plasma gradient become a backscatter issue.

III CONCLUSIONS

After researching the air chemistry, electromagnetic properties, and plasma generation mechanisms, SRI concludes that a plasma cloaking device will work and is feasible. Additional basic research issues remain to be resolved on the cloaking device concept suggested in this report. Researchers in the future could:

- Refine the air chemistry model
- Discover better seed gas mixtures
- Develop more efficient ionization techniques
- Quantify time– and source–dependent electron density profiles
- Model scattering from time–dependent density profiles
- Develop better confinement membranes
- Discover ways to circumvent or slow rapid deionization in air
- Measure scattering and plasma absorption coefficients.

In addition, it is altogether possible that additional cloaking device concepts based on different physical principles exist and are simpler.

The cloaking device concept advanced in this report could be constructed using helium or argon, seeded with TMAE, photoionized with a UV flash lamp, and confined by a Mylar membrane. Scattering and absorption experiments could then be conducted using plane–wave illumination with free–space to plasma boundary conditions. This confinement membrane provides a way to generate a large volume of plasma and is easy to fabricate. A cylindrical or conical confinement membrane could also be used to generate a plasma antenna [32].

Applications of plasma absorber are those for which carbon–based absorber is currently used. For applications in which the reflection from the tines of pyramid or wedge absorber is detrimental or the net absorption is insufficient, a plasma absorber offers an alternative with as much as a 40–dB improvement. The absorption per wavelength of a plasma absorber is superior to that of a carbon–based absorber and so offers a compact, lightweight alternative.

In addition to affording excellent reflection and absorption properties, a plasma absorber is switchable. This opens up the possibility for its use as a high–power absorber in transmission lines and antenna feeds to suppress ringing and reverberation in high–power pulsed radars and sounders. The scattering, diffraction, and radiation lobe characteristics of antennas could be altered by appropriate application of plasma absorber. These and other potential applications, such as an ionospheric mirror and plasma antenna, provided the basic motivation for this research contract.

Appendix A
ATMOSPHERIC REACTION RATES

The numeration system for the reactions in this Appendix continues the system adopted in previous SRI documentation for this project [1,2]. The reactions have been reorganized to group sequentially all the reactions relating to a single species. The index number preceding a reaction (such as A11 or F22) corresponds to the variable name A11 and F22 in the air chemistry code. Because the reactions were added sequentially without regard for species and then reorganized, the numeration in the following lists is not sequential. The 340 reactions below relate to the 44 species in Table A–1. All reaction rates were extracted from Bortner and Bauer [21] except for the ones followed by BA, which were extracted from Baulch et al. [33]. Reactions that have not yet been measured have been assigned a typical value extracted from Bortner and Bauer [21]. The units for two–body and three–body reactions are cm^3/s and cm^6/s, respectively.

Table A–1
SPECIES IN SIMULATION CODE

Neutral and Metastable	Positive	Negative
H, He, N, O	N^+, N_2^+, N_4^+	e
N_2, O_2, NO, OH	O^+, O_2^+, O_4^+	O^-, O_2^-, O_3^-, O_4^-
O_3	He^+, He_2^+	$O_2^- \bullet H_2O$
CO_2, H_2O, N_2O, NO_2	H_2O^+, H_3O^+	CO_3^-, CO_4^-
$He(^3S_1)$	NO^+	$CO_3^- \bullet H_2O$, $CO_4^- \bullet H_2O$
$O(^1S)$, $O(^1D)$	$O_2^+ \bullet H_2O$	
$N(^2P^o)$, $N(^2D^o)$	$H_3O^+ \bullet H_2O$	
$O_2(a^1\Delta_g)$, $O_2(b^1\Sigma_g^+)$	$H_3O^+ \bullet OH$	

A. NEGATIVE-ION REACTIONS

	Reaction	Rate
A1.	$e + O_2 \rightarrow O^- + O$	1.0E(–16)
A2.	$e + O_3 \rightarrow O^- + O_2$	9.0E(–12)
A3.	$e + O_2 + O_2 \rightarrow O_2^- + O_2$	$1.4E(-29)\ (300/T_e)\ \exp(-600/T_e)$
A4.	$e + O_2 + N_2 \rightarrow O_2^- + N_2$	1.0E(–31)
A5.	$e + O_2 + H_2O \rightarrow O_2^- + H_2O$	1.4E(–29)
A6.	$e + O_2 + CO_2 \rightarrow O_2^- + CO_2$	3.3E(–30)
A7.	$e + O_2 + He \rightarrow O_2^- + He$	1.0E(–31)
A132.	$e + He(^3S_1) \rightarrow He + e$	$7.0E(-10)(T_e/300)^{1/2}$
A8.	$O^- + O \rightarrow O_2 + e$	2.0E(–10)
A9.	$O^- + N \rightarrow NO + e$	2.0E(–10)
A10.	$O^- + O_2 \rightarrow O_3 + e$	5.0E(–15)
A11.	$O^- + O_2(a^1\Delta_g) \rightarrow O_3 + e$	3.0E(–10)
A12.	$O^- + O_2(a^1\Delta_g) \rightarrow O_2^- + O$	1.0E(–10)
A13.	$O^- + O_3 \rightarrow O_3^- + O$	5.3E(–10)
A14.	$O^- + N_2 \rightarrow N_2O + e$	1.0E(–14)
A15.	$O^- + NO \rightarrow NO_2 + e$	$2.5E(-10)\ (300/T_e)^{0.8}$
A16.	$O^- + O_2 + O_2 \rightarrow O_3^- + O_2$	1.0E(–30)
A17.	$O^- + O_2 + CO_2 \rightarrow CO_3^- + O_2$	$3.1E(-28)\ (300/T_e)$
A18.	$O^- + O_2 + He \rightarrow O_3^- + He$	1.0E(–30)
A64.	$O^- + O_2(b^1\Sigma_g^+) \rightarrow O + O_2 + e$	1.0E(–10)
A76.	$O^- + O(^1D) \rightarrow O + O + e$	1.0E(–10)
A89.	$O^- + N(^2D^o) \rightarrow O + N + e$	1.0E(–10)

A105.	$O^- + N(^2P^o) \rightarrow O + N + e$	1.0E(−10)
A122.	$O^- + O(^1S) \rightarrow O + O + e$	1.0E(−10)
A123.	$O^- + He(^3S_1) \rightarrow O + He + e$	3.0E(−10)
A19.	$O_2^- + O \rightarrow O^- + O_2$	1.5E(−10)
A20.	$O_2^- + N \rightarrow NO_2 + e$	3.0E(−10)
A21.	$O_2^- + N \rightarrow O^- + NO$	1.0E(−10)
A22.	$O_2^- + O_2 \rightarrow O_2 + O_2 + e$	$2.7E(-10)\ (T_{O_2^-}/300)^{0.5} \times \exp(-5590/T_{O_2^-})$
A23.	$O_2^- + O_2(a^1\Delta_g) \rightarrow O_2 + O_2 + e$	2.0E(−10)
A124.	$O_2^- + He(^3S_1) \rightarrow O_2 + He + e$	3.0E(−10)
A24.	$O_2^- + O_3 \rightarrow O_2 + O_3^-$	4.0E(−10)
A25.	$O_2^- + N_2 \rightarrow O_2 + N_2 + e$	$1.9E(-12)\ (T_{O_2^-}/300)^{1.5} \times \exp(-4990/T_{O_2^-})$
A26.	$O_2^- + O_2 + O_2 \rightarrow O_4^- + O_2$	$3.5E(-31)\ (300/T_{air})$
A27.	$O_2^- + O_2 + H_2O \rightarrow O_2^- \bullet H_2O + O_2$	$3.0E(-28)\ (300/T_{air})$
A28.	$O_2^- + O_2 + CO_2 \rightarrow CO_4^- + O_2$	$4.7E(-29)\ (300/T_{air})$
A29.	$O_2^- + O_2 + He \rightarrow O_4^- + He$	$3.5E(-31)\ (300/T_{air})$
A63.	$O_2^- + O_2(b^1\Sigma_g^+) \rightarrow O_2 + O_2 + e$	1.0E(−10)
A75.	$O_2^- + O(^1D) \rightarrow O_2 + O + e$	1.0E(−10)
A88.	$O_2^- + N(^2D^o) \rightarrow O_2 + N + e$	1.0E(−10)
A104.	$O_2^- + N(^2P^o) \rightarrow O_2 + N + e$	1.0E(−10)
A120.	$O_2^- + O(^1S) \rightarrow O^- + O + O$	1.0E(−10)
A121.	$O_2^- + O(^1S) \rightarrow O_2 + O + e$	1.0E(−10)

A30.	$O_3^- + O \rightarrow O_2 + O_2 + e$	1.0E(–11)
A31.	$O_3^- + O \rightarrow O_2^- + O_2$	3.2E(–10)
A32.	$O_3^- + CO_2 \rightarrow CO_3^- + O_2$	$5.5E(-10)\ (300/T_{air})^{0.49}$
A54.	$O_3^- + O_2(b^1\Sigma_g^+) \rightarrow O^- + O_2 + O_2$	1.0E(–10)
A65.	$O_3^- + O(^1D) \rightarrow O^- + O_2 + O$	1.0E(–10)
A77.	$O_3^- + N(^2D^o) \rightarrow O^- + O_2 + N$	1.0E(–10)
A78.	$O_3^- + N(^2D^o) \rightarrow O_3 + N + e$	1.0E(–10)
A90.	$O_3^- + N(^2P^o) \rightarrow O^- + O_2 + N$	1.0E(–10)
A91.	$O_3^- + N(^2P^o) \rightarrow O_2^- + O + N$	1.0E(–10)
A92.	$O_3^- + N(^2P^o) \rightarrow O_3 + N + e$	1.0E(–10)
A106.	$O_3^- + O(^1S) \rightarrow O^- + O_2 + O$	1.0E(–10)
A107.	$O_3^- + O(^1S) \rightarrow O_2^- + O + O$	1.0E(–10)
A108.	$O_3^- + O(^1S) \rightarrow O_3 + O + e$	1.0E(–10)
A125.	$O_3^- + He(^3S_1) \rightarrow O_2 + O + He + e$	3.0E(–10)
A33.	$O_4^- + O \rightarrow O_3^- + O_2$	4.0E(–10)
A34.	$O_4^- + O_2 \rightarrow O_2^- + O_2 + O_2$	2.7E(–14)
A35.	$O_4^- + O_3 \rightarrow O_3^- + O_2 + O_2$	3.0E(–10)
A36.	$O_4^- + CO_2 \rightarrow CO_4^- + O_2$	4.3E(–10)
A37.	$O_4^- + H_2O \rightarrow O_2^- \bullet H_2O + O_2$	1.4E(–9)
A49.	$O_4^- + O_2(a^1\Delta_g) \rightarrow O_2^- + O_2 + O_2$	1.0E(–10)
A59.	$O_4^- + O_2(b^1\Sigma_g^+) \rightarrow O_2^- + O_2 + O_2$	1.0E(–10)
A60.	$O_4^- + O_2(b^1\Sigma_g^+) \rightarrow O_2 + O_2 + O_2 + e$	1.0E(–10)
A71.	$O_4^- + O(^1D) \rightarrow O_2^- + O_2 + O$	1.0E(–10)
A72.	$O_4^- + O(^1D) \rightarrow O_2 + O_2 + O + e$	1.0E(–10)

A84.	$O_4^- + N(^2D^o) \rightarrow O_2^- + O_2 + N$	1.0E(−10)
A85.	$O_4^- + N(^2D^o) \rightarrow O_2 + O_2 + N + e$	1.0E(−10)
A99.	$O_4^- + N(^2P^o) \rightarrow O_2^- + O_2 + N$	1.0E(−10)
A100.	$O_4^- + N(^2P^o) \rightarrow O_2 + O_2 + N + e$	1.0E(−10)
A115.	$O_4^- + O(^1S) \rightarrow O_2^- + O_2 + O$	1.0E(−10)
A116.	$O_4^- + O(^1S) \rightarrow O_2 + O_2 + O + e$	1.0E(−10)
A126.	$O_4^- + He(^3S_1) \rightarrow O_2 + O_2 + He + e$	3.0E(−10)
A38.	$O_2^-\bullet H_2O + O_3 \rightarrow O_3^- + O_2 + H_2O$	2.3E(−10)
A39.	$O_2^-\bullet H_2O + CO_2 \rightarrow CO_4^- + H_2O$	5.8E(−10)
A51.	$O_2^-\bullet H_2O + O_2(a^1\Delta_g) \rightarrow O_2^- + H_2O + O_2$	1.0E(−10)
A55.	$O_2^-\bullet H_2O + O_2(b^1\Sigma_g^+) \rightarrow O_2^- + H_2O + O_2$	1.0E(−10)
A56.	$O_2^-\bullet H_2O + O_2(b^1\Sigma_g^+) \rightarrow O_2 + H_2O + O_2 + e$	1.0E(−10)
A66.	$O_2^-\bullet H_2O + O(^1D) \rightarrow O_2^- + H_2O + O$	1.0E(−10)
A67.	$O_2^-\bullet H_2O + O(^1D) \rightarrow O_2 + H_2O + O + e$	1.0E(−10)
A79.	$O_2^-\bullet H_2O + N(^2D^o) \rightarrow O_2^- + H_2O + N$	1.0E(−10)
A80.	$O_2^-\bullet H_2O + N(^2D^o) \rightarrow O_2 + H_2O + N + e$	1.0E(−10)
A93.	$O_2^-\bullet H_2O + N(^2P^o) \rightarrow O_2^- + H_2O + N$	1.0E(−10)
A94.	$O_2^-\bullet H_2O + N(^2P^o) \rightarrow O_2 + H_2O + N + e$	1.0E(−10)
A109.	$O_2^-\bullet H_2O + O(^1S) \rightarrow O_2^- + H_2O + O$	1.0E(−10)
A110.	$O_2^-\bullet H_2O + O(^1S) \rightarrow O_2 + H_2O + O + e$	1.0E(−10)
A127.	$O_2^-\bullet H_2O + He(^3S_1) \rightarrow O_2 + H_2O + He + e$	3.0E(−10)
A40.	$CO_3^- + O \rightarrow O_2^- + CO_2$	1.1E(−10)
A41.	$CO_3^- + O_2 + H_2O \rightarrow CO_3^-\bullet H_2O + O_2$	1.0E(−28) $(300/T_{air})$
A133.	$CO_3^- + He + H_2O \rightarrow CO_3^-\bullet H_2O + He$	1.0E(−28) $(300/T_{air})$

A68.	$CO_3^- + O(^1D) \rightarrow O^- + CO_2 + O$	1.0E(–10)
A81.	$CO_3^- + N(^2D^o) \rightarrow O^- + CO_2 + N$	1.0E(–10)
A95.	$CO_3^- + N(^2P^o) \rightarrow O^- + CO_2 + N$	1.0E(–10)
A96.	$CO_3^- + N(^2P^o) \rightarrow O + CO_2 + N + e$	1.0E(–10)
A111.	$CO_3^- + O(^1S) \rightarrow O^- + CO_2 + O$	1.0E(–10)
A112.	$CO_3^- + O(^1S) \rightarrow O + CO_2 + O + e$	1.0E(–10)
A128.	$CO_3^- + He(^3S_1) \rightarrow CO_2 + O + He + e$	3.0E(–10)
A42.	$CO_4^- + O \rightarrow CO_3^- + O_2$	1.5E(–10)
A43.	$CO_4^- + O_2 \rightarrow O_4^- + CO_2$	2.0E(–14)
A44.	$CO_4^- + O_3 \rightarrow O_3^- + CO_2 + O_2$	1.3E(–10)
A45.	$CO_4^- + N_2 + H_2O \rightarrow CO_4^-\bullet H_2O + N_2$	5.0E(–29) $(300/T_{air})$
A134.	$CO_4^- + He + H_2O \rightarrow CO_4^-\bullet H_2O + He$	5.0E(–29) $(300/T_{air})$
A46.	$CO_4^- + H_2O \rightarrow O_2^-\bullet H_2O + CO_2$	2.0E(–10)
A50.	$CO_4^- + O_2(a^1\Delta_g) \rightarrow O_2^- + CO_2 + O_2$	1.0E(–10)
A57.	$CO_4^- + O_2(b^1\Sigma_g^+) \rightarrow O_2^- + CO_2 + O_2$	1.0E(–10)
A58.	$CO_4^- + O_2(b^1\Sigma_g^+) \rightarrow O_2 + CO_2 + O_2 + e$	1.0E(–10)
A69.	$CO_4^- + O(^1D) \rightarrow O_2^- + CO_2 + O$	1.0E(–10)
A70.	$CO_4^- + O(^1D) \rightarrow O_2 + CO_2 + O + e$	1.0E(–10)
A82.	$CO_4^- + N(^2D^o) \rightarrow O_2^- + CO_2 + N$	1.0E(–10)
A83.	$CO_4^- + N(^2D^o) \rightarrow O_2 + CO_2 + N + e$	1.0E(–10)
A97.	$CO_4^- + N(^2P^o) \rightarrow O_2^- + CO_2 + N$	1.0E(–10)
A98.	$CO_4^- + N(^2P^o) \rightarrow O_2 + CO_2 + N + e$	1.0E(–10)
A113.	$CO_4^- + O(^1S) \rightarrow O_2^- + CO_2 + O$	1.0E(–10)
A114.	$CO_4^- + O(^1S) \rightarrow O_2 + CO_2 + O + e$	1.0E(–10)
A129.	$CO_4^- + He(^3S_1) \rightarrow CO_2 + O_2 + He + e$	3.0E(–10)

A47.	$CO_3^-\bullet H_2O + N_2 \rightarrow CO_3^- + H_2O + N_2$	3.0E(−14)
A52.	$CO_3^-\bullet H_2O + O_2(a^1\Delta_g) \rightarrow CO_3^- + H_2O + O_2$	1.0E(−10)
A61.	$CO_3^-\bullet H_2O + O_2(b^1\Sigma_g^+) \rightarrow CO_3^- + H_2O + O_2$	1.0E(−10)
A73.	$CO_3^-\bullet H_2O + O(^1D) \rightarrow CO_3^- + H_2O + O$	1.0E(−10)
A86.	$CO_3^-\bullet H_2O + N(^2D^o) \rightarrow CO_3^- + H_2O + N$	1.0E(−10)
A101.	$CO_3^-\bullet H_2O + N(^2P^o) \rightarrow CO_3^- + H_2O + N$	1.0E(−10)
A102.	$CO_3^-\bullet H_2O + N(^2P^o) \rightarrow CO_2 + H_2O + N + O + e$	1.0E(−10)
A117.	$CO_3^-\bullet H_2O + O(^1S) \rightarrow CO_3^- + H_2O + O$	1.0E(−10)
A118.	$CO_3^-\bullet H_2O + O(^1S) \rightarrow CO_2 + H_2O + O + O + e$	1.0E(−10)
A130.	$CO_3^-\bullet H_2O + He(^3S_1) \rightarrow CO_2 + O + H_2O + He + e$	3.0E(−10)

A48.	$CO_4^-\bullet H_2O + N_2 \rightarrow CO_4^- + H_2O + N_2$	1.0E(−14)
A53.	$CO_4^-\bullet H_2O + O_2(a^1\Delta_g) \rightarrow CO_4^- + H_2O + O_2$	1.0E(−10)
A62.	$CO_4^-\bullet H_2O + O_2(b^1\Sigma_g^+) \rightarrow CO_4^- + H_2O + O_2$	1.0E(−10)
A74.	$CO_4^-\bullet H_2O + O(^1D) \rightarrow CO_4^- + H_2O + O$	1.0E(−10)
A87.	$CO_4^-\bullet H_2O + N(^2D^o) \rightarrow CO_4^- + H_2O + N$	1.0E(−10)
A103.	$CO_4^-\bullet H_2O + N(^2P^o) \rightarrow CO_4^- + H_2O + N$	1.0E(−10)
A119.	$CO_4^-\bullet H_2O + O(^1S) \rightarrow CO_4^- + H_2O + O$	1.0E(−10)
A131.	$CO_4^-\bullet H_2O + He(^3S_1) \rightarrow CO_2 + O_2 + H_2O + He + e$	3.0E(−10)

B. POSITIVE-ION REACTIONS

Reaction	Rate
B1. $N^+ + O_2 \rightarrow N + O_2^+$	3.0E(–10)
B2. $N^+ + O_2 \rightarrow NO^+ + O$	2.8E(–10)
B3. $N^+ + H_2O \rightarrow H_2O^+ + N$	2.6E(–9)
B4. $N_2^+ + O \rightarrow NO^+ + N$	1.3E(–10) $(300/T_{air})^{0.46}$
B5. $N_2^+ + N_2 + N_2 \rightarrow N_4^+ + N_2$	5.0E(–29)
B6. $N_2^+ + N_2 + He \rightarrow N_4^+ + He$	5.0E(–29)
B64. $N_2^+ + He(^3S_1) \rightarrow N^+ + N + He$	1.0E(–10)
B7. $N_4^+ + O_2 \rightarrow O_2^+ + N_2 + N_2$	4.0E(–10)
B33. $N_4^+ + O_2(a^1\Delta_g) \rightarrow N_2^+ + N_2 + O_2$	1.0E(–10)
B37. $N_4^+ + O_2(b^1\Sigma_g^+) \rightarrow N_2^+ + N_2 + O_2$	1.0E(–10)
B42. $N_4^+ + O(^1D) \rightarrow N_2^+ + N_2 + O$	1.0E(–10)
B47. $N_4^+ + N(^2D^o) \rightarrow N_2^+ + N_2 + N$	1.0E(–10)
B52. $N_4^+ + N(^2P^o) \rightarrow N_2^+ + N_2 + N$	1.0E(–10)
B57. $N_4^+ + O(^1S) \rightarrow N_2^+ + N_2 + O$	1.0E(–10)
B63. $N_4^+ + He(^3S_1) \rightarrow N^+ + N + N_2 + He$	1.0E(–10)
B8. $O^+ + O_2 \rightarrow O_2^+ + O$	2.0E(–11) $(300/T_{air})^{0.4}$
B9. $O^+ + H_2O \rightarrow H_2O^+ + O$	2.33E(–9)
B10. $O^+ + N_2 + N_2 \rightarrow NO^+ + N + N_2$	6.0E(–29) $(300/T_{air})^2$
B73. $O^+ + N_2 + He \rightarrow NO^+ + N + He$	6.0E(–29) $(300/T_{air})^2$

B11.	$O_2^+ + N \rightarrow NO^+ + O$	1.2E(−10)
B12.	$O_2^+ + O_2 + O_2 \rightarrow O_4^+ + O_2$	2.8E(−30)
B13.	$O_2^+ + O_2 + He \rightarrow O_4^+ + He$	2.8E(−30)
B14.	$O_2^+ + H_2O + N_2 \rightarrow O_2^+ \bullet H_2O + N_2$	$2.8E(-28)\ (300/T_{air})^2$
B62.	$O_2^+ + He(^3S_1) \rightarrow O^+ + O + He$	1.0E(−10)
B74.	$O_2^+ + H_2O + He \rightarrow O_2^+ \bullet H_2O + He$	$2.8E(-28)\ (300/T_{air})^2$
B15.	$O_4^+ + O \rightarrow O_2^+ + O_3$	3.0E(−10)
B16.	$O_4^+ + O_2(a^1\Delta_g) \rightarrow O_2^+ + O_2 + O_2$	1.0E(−10)
B17.	$O_4^+ + N_2 \rightarrow O_2^+ + O_2 + N_2$	$2.6E(-5)\ (300/T_{air})^{4.2} \times \exp(-5400/T_{air})$
B18.	$O_4^+ + H_2O \rightarrow O_2^+ \bullet H_2O + O_2$	1.5E(−9)
B39.	$O_4^+ + O_2(b^1\Sigma_g^+) \rightarrow O_2^+ + O_2 + O_2$	1.0E(−10)
B44.	$O_4^+ + O(^1D) \rightarrow O_2^+ + O_2 + O$	1.0E(−10)
B49.	$O_4^+ + N(^2D^o) \rightarrow O_2^+ + O_2 + N$	1.0E(−10)
B54.	$O_4^+ + N(^2P^o) \rightarrow O_2^+ + O_2 + N$	1.0E(−10)
B59.	$O_4^+ + O(^1S) \rightarrow O_2^+ + O_2 + O$	1.0E(−10)
B61.	$O_4^+ + He(^3S_1) \rightarrow O^+ + O + O_2 + He$	1.0E(−10)
B19.	$He^+ + N_2 \rightarrow N^+ + N + He$	6.0E(−10)
B20.	$He^+ + N_2 \rightarrow N_2^+ + He$	6.0E(−10)
B21.	$He^+ + O_2 \rightarrow O^+ + O + He$	6.0E(−10)
B22.	$He^+ + O_2 \rightarrow O_2^+ + He$	6.0E(−10)
B23.	$He^+ + He + He \rightarrow He_2^+ + He$	1.1E(−31)

B24.	$He_2^+ + N_2 \rightarrow N_2^+ + He + He$	1.2E(–9)
B60.	$He_2^+ + O_2 \rightarrow O_2^+ + He + He$	1.2E(–9)
B65.	$He_2^+ + He(^3S_1) \rightarrow He^+ + He + He$	1.0E(–10)
B68.	$NO^+ + He(^3S_1) \rightarrow N^+ + O + He$	5.0E(–11)
B71.	$NO^+ + He(^3S_1) \rightarrow O^+ + N + He$	5.0E(–11)
B25.	$O_2^+ \bullet H_2O + O_2 \rightarrow O_4^+ + H_2O$	9.4E(–14)
B26.	$O_2^+ \bullet H_2O + O_2(a^1\Delta_g) \rightarrow O_2^+ + H_2O + O_2$	1.0E(–10)
B27.	$O_2^+ \bullet H_2O + NO \rightarrow NO^+ + H_2O + O_2$	1.0E(–10)
B28.	$O_2^+ \bullet H_2O + H_2O \rightarrow H_3O^+ \bullet OH + O_2$	1.0E(–9)
B38.	$O_2^+ \bullet H_2O + O_2(b^1\Sigma_g^+) \rightarrow O_2^+ + H_2O + O_2$	1.0E(–10)
B43.	$O_2^+ \bullet H_2O + O(^1D) \rightarrow O_2^+ + H_2O + O$	1.0E(–10)
B48.	$O_2^+ \bullet H_2O + N(^2D^o) \rightarrow O_2^+ + H_2O + N$	1.0E(–10)
B53.	$O_2^+ \bullet H_2O + N(^2P^o) \rightarrow O_2^+ + H_2O + N$	1.0E(–10)
B58.	$O_2^+ \bullet H_2O + O(^1S) \rightarrow O_2^+ + H_2O + O$	1.0E(–10)
B69	$O_2^+ \bullet H_2O + He(^3S_1) \rightarrow O^+ + O + H_2O + He$	1.0E(–10)
B29.	$H_2O^+ + O_2 \rightarrow O_2^+ + H_2O$	2.0E(–10)
B30.	$H_2O^+ + H_2O \rightarrow H_3O^+ + OH$	1.8E(–9)
B66.	$H_2O^+ + He(^3S_1) \rightarrow O^+ + 2H + He$	1.0E(–10)
B31.	$H_3O^+ + H_2O + N_2 \rightarrow H_3O^+ \bullet H_2O + N_2$	3.4E(–27)
B67.	$H_3O^+ + He(^3S_1) \rightarrow O^+ + 3H + He$	1.0E(–10)
B75.	$H_3O^+ + H_2O + He \rightarrow H_3O^+ \bullet H_2O + He$	3.4E(–27) $(300/T_{air})^2$

B32.	$H_3O^+ \bullet OH + H_2O \rightarrow H_3O^+ \bullet H_2O + OH$	1.0E(–9)
B34.	$H_3O^+ \bullet OH + O_2(a^1\Delta_g) \rightarrow H_3O^+ + OH + O_2$	1.0E(–10)
B36.	$H_3O^+ \bullet OH + O_2(b^1\Sigma_g^+) \rightarrow H_3O^+ + OH + O_2$	1.0E(–10)
B41.	$H_3O^+ \bullet OH + O(^1D) \rightarrow H_3O^+ + OH + O$	1.0E(–10)
B46.	$H_3O^+ \bullet OH + N(^2D^o) \rightarrow H_3O^+ + OH + N$	1.0E(–10)
B51.	$H_3O^+ \bullet OH + N(^2P^o) \rightarrow H_3O^+ + OH + N$	1.0E(–10)
B56.	$H_3O^+ \bullet OH + O(^1S) \rightarrow H_3O^+ + OH + O$	1.0E(–10)
B72.	$H_3O^+ \bullet OH + He(^3S_1) \rightarrow O^+ + 3H + OH + He$	1.0E(–10)
B35.	$H_3O^+ \bullet H_2O + O_2(b^1\Sigma_g^+) \rightarrow H_3O^+ + H_2O + O_2$	1.0E(–10)
B40.	$H_3O^+ \bullet H_2O + O(^1D) \rightarrow H_3O^+ + H_2O + O$	1.0E(–10)
B45.	$H_3O^+ \bullet H_2O + N(^2D^o) \rightarrow H_3O^+ + H_2O + N$	1.0E(–10)
B50.	$H_3O^+ \bullet H_2O + N(^2P^o) \rightarrow H_3O^+ + H_2O + N$	1.0E(–10)
B55.	$H_3O^+ \bullet H_2O + O(^1S) \rightarrow H_3O^+ + H_2O + O$	1.0E(–10)
B70.	$H_3O^+ \bullet H_2O + He(^3S_1) \rightarrow O^+ + 3H + H_2O + He$	1.0E(–10)

C. NEUTRAL–SPECIES REACTIONS

Reaction	Rate
C1. $N + N + N_2 \rightarrow N_2 + N_2$	$7.6E(-34)\ \exp(500/T_{air})$
C31. $N + N + He \rightarrow N_2 + He$	$7.6E(-34)\ \exp(500/T_{air})$
C2. $O + O + N_2 \rightarrow O_2 + N_2$	$3.0E(-33)\ (300/T_{air})^{2.9}$
C32. $O + O + He \rightarrow O_2 + He$	$3.0E(-33)\ (300/T_{air})^{2.9}$
C3. $O + O_2 + N_2 \rightarrow O_3 + N_2$	$5.5E(-34)\ (300/T_{air})^{2.6}$
C33. $O + O_2 + He \rightarrow O_3 + He$	$5.5E(-34)\ (300/T_{air})^{2.6}$

C7.	$O^3 + O_2(b^1\Sigma_g^+) \rightarrow O_2 + O_2 + O$	2.2E(−11)	BA
C8.	$O^3 + O(^1D) \rightarrow O_2 + O_2$	1.2E(−10)	BA
C9.	$O^3 + O(^1D) \rightarrow O_2 + O + O$	1.2E(−10)	BA
C10.	$O^3 + N(^2D^o) \rightarrow O_2 + N + O$	1.0E(−10)	
C11.	$O^3 + N(^2P^o) \rightarrow O_2 + N + O$	1.0E(−10)	
C12.	$O^3 + O(^1S) \rightarrow O_2 + O + O$	1.0E(−10)	
C13.	$N_2O + O(^1D) \rightarrow N_2 + O + O$	1.0E(−10)	
C14.	$N_2O + O(^1D) \rightarrow 2NO$	6.6E(−11)	BA
C15.	$N_2O + N(^2D^o) \rightarrow N_2 + N + O$	1.0E(−10)	
C16.	$N_2O + N(^2P^o) \rightarrow N_2 + N + O$	1.0E(−10)	
C17.	$N_2O + O(^1S) \rightarrow N_2 + O + O$	1.0E(−10)	
C18.	$NO_2 + N(^2P^o) \rightarrow NO + O + N$	1.0E(−10)	
C19.	$NO_2 + O(^1S) \rightarrow NO + O + O$	1.0E(−10)	
C4.	$O_2(a^1\Delta_g) + O_2 \rightarrow O_2 + O_2$	2.4E(−18)	
C5.	$O_2(a^1\Delta_g) + N_2 \rightarrow O_2 + N_2$	1.1E(−19)	
C6.	$O_2(a^1\Delta_g) + H_2O \rightarrow O_2 + H_2O$	1.5E(−17)	
C20.	$O_2(b^1\Sigma_g^+) + N_2 \rightarrow O_2 + N_2$	2.0E(−15)	BA
C21.	$O_2(b^1\Sigma_g^+) + O_2 \rightarrow O_2 + O_2$	4.0E(−17)	BA
C22.	$O_2(b^1\Sigma_g^+) + H_2O \rightarrow O_2 + H_2O$	4.0E(−12)	BA

C23.	$O(^1D) + N_2 \rightarrow O + N_2$	$1.8E(-11)\ \exp(107/T_{air})$	BA
C24.	$O(^1D) + O_2 \rightarrow O + O_2$	$3.2E(-11)\ \exp(67/T_{air})$	BA
C25.	$O(^1D) + H_2O \rightarrow 2OH$	$2.3E(-10)$	BA
C26.	$He(^3S_1) + He(^3S_1) \rightarrow He_2^+ + e$	$2.0E(-9)$	
C27.	$He(^3S_1) + He(^3S_1) \rightarrow He^+ + He + e$	$2.0E(-9)$	
C28.	$He(^3S_1) + N_2 \rightarrow N^+ + N + He + e$	$1.0E(-10)$	
C29.	$He(^3S_1) + O_2 \rightarrow O^+ + O + He + e$	$1.0E(-10)$	
C30.	$He(^3S_1) + H_2O \rightarrow H_2O^+ + He + e$	$1.0E(-10)$	

D. POSITIVE–ION ELECTRON RECOMBINATION

Reaction		Rate
D1.	$N^+ + e + e \rightarrow N + e$	$7.0E(-20)\ (300/T_e)^{4.5}$
D2.	$N^+ + e + N_2 \rightarrow N + N_2$	$6.0E(-27)\ (300/T_e)^{2.5}$
D28.	$N^+ + e + He \rightarrow N + He$	$6.0E(-27)\ (300/T_e)^{2.5}$
D3.	$N_2^+ + e + e \rightarrow N_2 + e$	$7.0E(-20)\ (300/T_e)^{4.5}$
D4.	$N_2^+ + e \rightarrow N + N$	$2.7E(-7)\ (300/T_e)^{0.2}$
D24.	$N_4^+ + e + e \rightarrow N_2 + N_2 + e$	$7.0E(-20)\ (300/T_e)^{4.5}$
D5.	$N_4^+ + e \rightarrow N_2 + N_2$	$2.0E(-6)$
D6.	$O^+ + e + e \rightarrow O + e$	$7.0E(-20)\ (300/T_e)^{4.5}$
D7.	$O^+ + e + O_2 \rightarrow O + O_2$	$6.0E(-27)\ (300/T_e)^{2.5}$
D29.	$O^+ + e + He \rightarrow O + He$	$6.0E(-27)\ (300/T_e)^{2.5}$

D8.	$O_2^+ + e + e \rightarrow O_2 + e$	$7.0E(-20)\ (300/T_e)^{4.5}$
D9.	$O_2^+ + e \rightarrow O + O$	$2.1E(-7)\ (300/T_e)^{0.7}$
D25.	$O_4^+ + e + e \rightarrow O_2 + O_2 + e$	$7.0E(-20)\ (300/T_e)^{4.5}$
D10.	$O_4^+ + e \rightarrow O + O + O_2$	$2.0E(-6)$
D11.	$He^+ + e + e \rightarrow He + e$	$1.0E(-19)$
D27.	$He^+ + e + e \rightarrow He(^3S_1) + e$	$3.0E(-20)\ (300/T_e)^{4.5}$
D23.	$He_2^+ + e + e \rightarrow He + He + e$	$7.0E(-20)\ (300/T_e)^{4.5}$
D12.	$He_2^+ + e \rightarrow He + He$	$1.0E(-8)$
D13.	$He_2^+ + e + He \rightarrow 3He$	$2.0E(-27)$
D14.	$NO^+ + e + e \rightarrow NO + e$	$7.0E(-20)\ (300/T_e)^{4.5}$
D15.	$NO^+ + e \rightarrow N + O$	$4.0E(-7)\ (300/T_e)^{0.4}$
D16.	$H_3O^+ + e + e \rightarrow H_2O + H + e$	$7.0E(-20)\ (300/T_e)^{4.5}$
D17.	$H_3O^+ + e \rightarrow H_2O + H$	$1.3E(-6)\ (300/T_e)^{1.0}$
D26.	$O_2^+ \bullet H_2O + e + e \rightarrow O_2 + H_2O + e$	$7.0E(-20)\ (300/T_e)^{4.5}$
D18.	$O_2^+ \bullet H_2O + e \rightarrow O_2 + H_2O$	$1.5E(-6)\ (300/T_e)^{0.2}$
D19.	$H_3O^+ \bullet OH + e + e \rightarrow H_2O + OH + H + e$	$7.0E(-20)\ (300/T_e)^{4.5}$
D20.	$H_3O^+ \bullet OH + e \rightarrow H_2O + OH + H$	$2.0E(-6)\ (300/T_e)^{0.2}$

D21.	$H_3O^+ \bullet H_2O + e + e \rightarrow 2H_2O + H + e$	$7.0E(-20)\ (300/T_e)^{4.5}$
D22.	$H_3O^+ \bullet H_2O + e \rightarrow 2H_2O + H$	$2.8E(-6)\ (300/T_e)^{0.15}$

E. TWO-BODY POSITIVE-ION NEGATIVE-ION RECOMBINATION

Reaction		Rate
E1.	$N^+ + O^- \rightarrow N + O$	$2.6E(-7)\ (300/T_{air})^{0.5}$
E2.	$N_2^+ + O_2^- \rightarrow N_2 + O_2$	$1.6E(-7)\ (300/T_{air})^{0.5}$
E3.	$O^+ + O^- \rightarrow O + O$	$2.7E(-7)\ (300/T_{air})^{0.5}$
E4.	$O_2^+ + O^- \rightarrow O_2 + O$	$1.0E(-7)\ (300/T_{air})^{0.5}$
E5.	$O_2^+ + O_2^- \rightarrow O_2 + O_2$	$4.2E(-7)\ (300/T_{air})^{0.5}$
E6.	$NO^+ + O^- \rightarrow NO + O$	$4.9E(-7)\ (300/T_{air})^{0.5}$
E7.	$NO^+ + O_2^- \rightarrow NO + O_2$	$6.0E(-7)\ (300/T_{air})^{0.5}$

F. THREE–BODY CLUSTER–ION RECOMBINATION

The estimate cited by Bortner and Bauer [21] for the three–body cluster–ion recombination rate is 1.0E(–25) $(300/T_{air})^{5/2}$ where the third body is N_2 or the dominant gas species. Because little information is available for individual reactions, the reaction rate for all the following reactions is assumed to be the same.

	Reaction
F1.	$O_2^+ + O_3^- + N_2 \rightarrow 2O_2 + O + N_2$
F2.	$O_2^+ + O_4^- + N_2 \rightarrow 3O_2 + N_2$
F3.	$O_2^+ + CO_3^- + N_2 \rightarrow O_2 + CO_2 + O + N_2$
F4.	$O_2^+ + CO_4^- + N_2 \rightarrow 2O_2 + CO_2 + N_2$
F5.	$O_2^+ + O_2^-\bullet H_2O + N_2 \rightarrow 2O_2 + H_2O + N_2$
F32.	$O_2^+ + O_3^- + He \rightarrow 2O_2 + O + He$
F33.	$O_2^+ + O_4^- + He \rightarrow 3O_2 + He$
F34.	$O_2^+ + CO_3^- + He \rightarrow O_2 + CO_2 + O + He$
F35.	$O_2^+ + CO_4^- + He \rightarrow 2O_2 + CO_2 + He$
F36.	$O_2^+ + O_2^-\bullet H_2O + He \rightarrow 2O_2 + H_2O + He$
F6.	$O_4^+ + O^- + N_2 \rightarrow 2O_2 + O + N_2$
F7.	$O_4^+ + O_2^- + N_2 \rightarrow 3O_2 + N_2$
F8.	$O_4^+ + O_3^- + N_2 \rightarrow 2O_2 + O_3 + N_2$
F9.	$O_4^+ + O_4^- + N_2 \rightarrow 4O_2 + N_2$

F37. $O_4^+ + O^- + He \rightarrow 2O_2 + O + He$

F38. $O_4^+ + O_2^- + He \rightarrow 3O_2 + He$

F39. $O_4^+ + O_3^- + He \rightarrow 2O_2 + O_3 + He$

F40. $O_4^+ + O_4^- + He \rightarrow 4O_2 + He$

F10. $NO^+ + O_3^- + N_2 \rightarrow NO + O_2 + O + N_2$

F11. $NO^+ + O_4^- + N_2 \rightarrow NO + 2O_2 + N_2$

F12. $NO^+ + CO_3^- + N_2 \rightarrow NO + CO_2 + O + N_2$

F13. $NO^+ + CO_4^- + N_2 \rightarrow NO + CO_2 + O_2 + N_2$

F14. $NO^+ + O_2^- \bullet H_2O + N_2 \rightarrow NO + H_2O + O + N_2$

F15. $NO^+ + CO_3^- \bullet H_2O + N_2 \rightarrow NO + H_2O + CO_2 + O + N_2$

F16. $NO^+ + CO_4^- \bullet H_2O + N_2 \rightarrow NO + H_2O + CO_2 + O_2 + N_2$

F41. $NO^+ + O_3^- + He \rightarrow NO + O_2 + O + He$

F42. $NO^+ + O_4^- + He \rightarrow NO + 2O_2 + He$

F43. $NO^+ + CO_3^- + He \rightarrow NO + CO_2 + O + He$

F44. $NO^+ + CO_4^- + He \rightarrow NO + CO_2 + O_2 + He$

F45. $NO^+ + O_2^- \bullet H_2O + He \rightarrow NO + H_2O + O + He$

F46. $NO^+ + CO_3^- \bullet H_2O + He \rightarrow NO + H_2O + CO_2 + O + He$

F47. $NO^+ + CO_4^- \bullet H_2O + He \rightarrow NO + H_2O + CO_2 + O_2 + He$

F17. $O_2^+ \bullet H_2O + O^- + N_2 \rightarrow O_2 + H_2O + O + N_2$

F18. $O_2^+ \bullet H_2O + O_2^- + N_2 \rightarrow 2O_2 + H_2O + N_2$

F19. $O_2^+ \bullet H_2O + O_3^- + N_2 \rightarrow O_2 + O_3 + H_2O + N_2$

F20. $O_2^+ \bullet H_2O + CO_3^- + N_2 \rightarrow O_2 + O + H_2O + CO_2 + N_2$

F21. $O_2^+ \bullet H_2O + CO_4^- + N_2 \rightarrow 2O_2 + H_2O + CO_2 + N_2$

F22. $O_2^+ \bullet H_2O + O_2^- \bullet H_2O + N_2 \rightarrow 2O_2 + 2H_2O + N_2$

F48. $O_2^+ \bullet H_2O + O^- + He \rightarrow O_2 + H_2O + O + He$

F49. $O_2^+ \bullet H_2O + O_2^- + He \rightarrow 2O_2 + H_2O + He$

F50. $O_2^+ \bullet H_2O + O_3^- + He \rightarrow O_2 + O_3 + H_2O + He$

F51. $O_2^+ \bullet H_2O + CO_3^- + He \rightarrow O_2 + O + H_2O + CO_2 + He$

F52. $O_2^+ \bullet H_2O + CO_4^- + He \rightarrow 2O_2 + H_2O + CO_2 + He$

F53. $O_2^+ \bullet H_2O + O_2^- \bullet H_2O + He \rightarrow 2O_2 + 2H_2O + He$

F23. $H_3O^+ \cdot H_2O + O^- + N_2 \rightarrow 2H_2O + OH + N_2$

F24. $H_3O^+ \cdot H_2O + O_2^- + N_2 \rightarrow 2H_2O + OH + O + N_2$

F25. $H_3O^+ \cdot H_2O + O_3^- + N_2 \rightarrow 2H_2O + OH + O_2 + N_2$

F26. $H_3O^+ \cdot H_2O + O_4^- + N_2 \rightarrow 2H_2O + CH + O_3 + N_2$

F27. $H_3O^+ \cdot H_2O + CO_3^- + N_2 \rightarrow 2H_2O + OH + CO_2 + N_2$

F28. $H_3O^+ \cdot H_2O + CO_4^- + N_2 \rightarrow 2H_2O + OH + CO_2 + O + N_2$

F29. $H_3O^+ \cdot H_2O + O_2^- \cdot H_2O + N_2 \rightarrow 3H_2O + OH + O + N_2$

F30. $H_3O^+ \cdot H_2O + CO_3^- \cdot H_2O + N_2 \rightarrow 3H_2O + OH + CO_2 + N_2$

F31. $H_3O^+ \cdot H_2O + CO_4^- \cdot H_2O + N_2 \rightarrow 3H_2O + OH + CO_2 + O + N_2$

F54. $H_3O^+ \cdot H_2O + O^- + He \rightarrow 2H_2O + OH + He$

F55. $H_3O^+ \cdot H_2O + O_2^- + He \rightarrow 2H_2O + CH + O + He$

F56. $H_3O^+ \cdot H_2O + O_3^- + He \rightarrow 2H_2O + OH + O_2 + He$

F57. $H_3O^+ \cdot H_2O + O_4^- + He \rightarrow 2H_2O + OH + O_3 + He$

F58. $H_3O^+ \cdot H_2O + CO_3^- + He \rightarrow 2H_2O + OH + CO_2 + He$

F59. $H_3O^+ \cdot H_2O + CO_4^- + He \rightarrow 2H_2O + OH + CO_2 + O + He$

F60. $H_3O^+ \cdot H_2O + O_2^- \cdot H_2O + He \rightarrow 3H_2O + OH + O + He$

F61. $H_3O^+ \cdot H_2O + CO_3^- \cdot H_2O + He \rightarrow 3H_2O + OH + CO_2 + He$

F62. $H_3O^+ \cdot H_2O + CO_4^- \cdot H_2O + He \rightarrow 3H_2O + OH + CO_2 + O + He$

Appendix B

PLASMA LIFETIME DATA

The data in Tables B–1 through B–4 correspond to the plasma lifetime of helium with air as an impurity and of air from sea level to 300,000 ft. These data are plotted in Figures 2 – 5 of Reference 14 (copy attached). The numerical values in these tables provide backup and constitute a database to validate the installation of AIR.EXE.

Table B–1
PLASMA LIFETIME IN HELIUM WITH 100 ppm AIR

Pressure (torr)	Lifetime versus Electron Number Density				
	10^{15}/cc	10^{14}	10^{13}	10^{12}	10^{11}
1000	617 ps	39.8 ns	736 ns	7.4 μs	25.1 μs
760	614 ps	39.8 ns	926 ns	9.3 μs	29.3 μs
500	613 ps	34.1 ns	1.2 μs	12.6 μs	36.9 μs
200	611 ps	29.3 ns	2.5 μs	23.3 μs	68.1 μs
100	611 ps	27.1 ns	2.5 μs	36.9 μs	117 μs
50	–	27.1 ns	2.9 μs	58.4 μs	200 μs
20	–	27.1 ns	3.2 μs	108 μs	369 μs
10	–	27.1 ns	3.2 μs	159 μs	631 μs
Pressure (torr)	Lifetime versus Electron Number Density				
	10^{10}/cc	10^{9}	10^{8}	10^{7}	10^{6}
1000	117 μs	342 μs	584 μs	631 μs	631 μs
760	136 μs	464 μs	926 μs	1.1 ms	1.1 ms
500	159 μs	736 μs	1.8 μs	2.5 ms	2.5 ms
200	251 μs	1.3 ms	5.4 μs	12.6 ms	15.8 ms
100	398 μs	1.7 ms	10.0 μs	31.6 ms	58.4 ms
50	631 μs	2.5 ms	13.6 μs	68.1 ms	171 ms
20	1.1 ms	5.0 ms	20.0 μs	126 ms	541 ms
10	1.6 ms	7.9 ms	31.6 μs	159 ms	926 ms

Note: A dash denotes heating in excess of 50° C.

Table B-2

PLASMA LIFETIME IN HELIUM WITH 10 ppm AIR

Pressure (torr)	Lifetime versus Electron Number Density				
	10^{15}/cc	10^{14}	10^{13}	10^{12}	10^{11}
1000	616 ps	42.3 ns	1.8 μs	8.6 μs	73.6 μs
760	614 ps	39.3 ns	2.1 μs	10.8 μs	92.6 μs
500	612 ps	33.9 ns	2.6 μs	14.6 μs	126 μs
200	611 ps	29.0 ns	3.4 μs	26.1 μs	230 μs
100	611 ps	28.7 ns	3.9 μs	39.2 μs	313 μs
50	–	28.6 ns	3.6 μs	61.5 μs	271 μs
20	–	28.7 ns	3.4 μs	113 μs	365 μs
10	–	28.7 ns	3.3 μs	178 μs	627 μs
Pressure (torr)	Lifetime versus Electron Number Density				
	10^{10}/cc	10^{9}	10^{8}	10^{7}	10^{6}
1000	251 μs	1.2 ms	3.4 ms	5.8 ms	6.3 ms
760	293 μs	1.4 ms	4.6 ms	9.3 ms	10.8 ms
500	369 μs	1.6 ms	7.4 ms	18.5 ms	25.1 ms
200	681 μs	2.3 ms	12.6 ms	54.1 ms	126 ms
100	1.2 ms	3.7 ms	15.8 ms	92.6 ms	316 ms
50	1.9 ms	6.4 ms	23.3 ms	126 ms	631 ms
20	3.4 ms	10.8 ms	50.1 ms	171 ms	1.1 s
10	5.4 ms	15.4 ms	80.8 ms	316 ms	1.4 s

Note: A dash denotes heating in excess of 50° C.

Table B–3

PLASMA LIFETIME IN HELIUM WITH 1 ppm AIR

Pressure (torr)	Lifetime versus Electron Number Density				
	10^{15}/cc	10^{14}	10^{13}	10^{12}	10^{11}
1000	616 ps	42.3 ns	2.9 μs	27.0 μs	89.3 μs
760	614 ps	39.3 ns	3.1 μs	33.4 μs	112 μs
500	612 ps	33.9 ns	3.6 μs	45.1 μs	152 μs
200	611 ps	29.0 ns	4.2 μs	82.5 μs	267 μs
100	611 ps	28.7 ns	4.2 μs	116 μs	414 μs
50	–	28.6 ns	3.7 μs	152 μs	655 μs
20	–	28.7 ns	3.4 μs	184 μs	1.2 ms
10	–	28.6 ns	3.3 μs	226 μs	1.8 ms
Pressure (torr)	Lifetime versus Electron Number Density				
	10^{10}/cc	10^{9}	10^{8}	10^{7}	10^{6}
1000	760 μs	2.5 ms	11.3 ms	34.2 ms	58.4 ms
760	917 μs	2.9 ms	13.2 ms	47.3 ms	92.6 ms
500	1.3 ms	3.6 ms	15.8 ms	71.0 ms	175 ms
200	2.3 ms	6.9 ms	23.7 ms	124 ms	540 ms
100	2.9 ms	11.6 ms	37.5 ms	158 ms	923 ms
50	2.5 ms	18.4 ms	63.8 ms	229 ms	1.3 s
20	3.1 ms	32.9 ms	107 ms	498 ms	1.8 s
10	4.6 ms	46.3 ms	152 ms	809 ms	3.1 s

Note: A dash denotes heating in excess of 50° C.

Table B–4
PLASMA LIFETIME IN AIR

Altitude (kft)	Lifetime versus Electron Number Density				
	10^{15}/cc	10^{14}	10^{13}	10^{12}	10^{11}
0	613 ps	4.3 ns	8.6 ns	9.3 ns	9.3 ns
10	651 ps	7.4 ns	17.1 ns	20.0 ns	20.0 ns
20	662 ps	11.7 ns	31.6 ns	39.8 ns	43.0 ns
30	668 ps	17.1 ns	63.1 ns	79.4 ns	85.8 ns
40	679 ps	21.5 ns	117 ns	171 ns	200 ns
50	693 ps	23.3 ns	215 ns	398 ns	501 ns
60	702 ps	23.3 ns	369 ns	858 ns	1.3 μs
70	–	23.3 ns	501 ns	1.7 μs	2.9 μs
80	–	25.1 ns	631 ns	3.2 μs	6.8 μs
90	–	27.1 ns	681 ns	5.4 μs	13.6 μs
100	–	29.3 ns	631 ns	7.4 μs	25.1 μs
110	–	29.3 ns	631 ns	8.6 μs	43.0 μs
120	–	–	631 ns	8.6 μs	63.1 μs
130	–	–	681 ns	8.6 μs	73.6 μs
140	–	–	736 ns	7.9 μs	85.8 μs
150	–	–	736 ns	7.9 μs	85.8 μs
160	–	–	736 ns	7.9 μs	85.8 μs
170	–	–	794 ns	7.9 μs	85.8 μs
180	–	–	–	7.9 μs	79.4 μs
190	–	–	–	8.6 μs	79.4 μs
200	–	–	–	8.6 μs	79.4 μs
210	–	–	–	9.3 μs	79.4 μs
220	–	–	–	9.3 μs	85.8 μs
230	–	–	–	9.3 μs	85.8 μs
240	–	–	–	–	85.8 μs
250	–	–	–	–	85.8 μs
260	–	–	–	–	92.6 μs
270	–	–	–	–	92.6 μs
280	–	–	–	–	–
290	–	–	–	–	–
300	–	–	–	–	–

Note: A dash denotes heating in excess of 50° C.

Table B-4 (Concluded)

Altitude (kft)	Lifetime versus Electron Number Density				
	10^{10}/cc	10^{9}	10^{8}	10^{7}	10^{6}
0	9.3 ns	9.3 ns	9.3 ns	9.3 ns	9.3 ns
10	20.0 ns	20.0 ns	20.0 ns	20.0 ns	20.0 ns
20	43.0 ns	43.0 ns	43.0 ns	43.0 ns	43.0 ns
30	85.8 ns	85.8 ns	85.8 ns	85.8 ns	85.8 ns
40	200 ns	200 ns	200 ns	200 ns	200 ns
50	501 ns	501 ns	501 ns	501 ns	501 ns
60	1.4 μs	1.4 μs	1.4 μs	1.4 μs	1.4 μs
70	3.4 μs	3.4 μs	3.4 μs	3.4 μs	3.4 μs
80	8.6 μs	9.3 μs	9.3 μs	9.3 μs	9.3 μs
90	21.5 μs	23.3 μs	23.3 μs	23.3 μs	23.3 μs
100	46.4 μs	58.4 μs	63.1 μs	63.1 μs	63.1 μs
110	92.6 μs	147 μs	159 μs	159 μs	159 μs
120	171 μs	316 μs	398 μs	398 μs	398 μs
130	271 μs	541 μs	858 μs	1.0 ms	1.0 ms
140	369 μs	858 μs	1.7 ms	2.3 ms	2.3 ms
150	464 μs	1.3 ms	3.2 ms	5.0 ms	5.4 ms
160	584 μs	1.7 ms	4.6 ms	9.3 ms	11.7 ms
170	736 μs	2.7 ms	7.4 ms	17.1 ms	23.3 ms
180	926 μs	5.4 ms	13.6 ms	31.6 ms	46.4 ms
190	926 μs	7.9 ms	27.1 ms	58.4 ms	100 ms
200	858 μs	9.3 ms	46.4 ms	108 ms	184 ms
210	794 μs	9.3 ms	68.1 ms	200 ms	341 ms
220	794 μs	9.3 ms	85.8 ms	342 ms	681 ms
230	794 μs	8.6 ms	100 ms	584 ms	1.5 s
240	794 μs	8.6 ms	100 ms	794 ms	2.5 s
250	794 μs	7.9 ms	92.6 ms	926 ms	4.6 s
260	858 μs	7.9 ms	85.8 ms	1.0 s	7.9 s
270	858 μs	7.9 ms	79.4 ms	1.0 s	8.6 s
280	858 μs	7.9 ms	79.4 ms	926 ms	10.0 s
290	858 μs	7.9 ms	79.4 ms	858 ms	10.0 s
300	858 μs	7.9 ms	79.4 ms	794 ms	9.3 s

Appendix C

AIR CHEMISTRY CODE ORGANIZATION

The air chemistry code has been developed to run on an IBM AT computer equipped with a math coprocessor chip. The source code was developed using IBM FORTRAN, Ryan–McFarland Corp. version 1.22. The software provided as an attachment to this report includes source code, EXE files, and auxilary programs. It is on a high–density, 5¼–in., 96–TPI, 1.2–MB diskette and requires a 1.2–MB high–density disk drive.

The source code is provided to other researchers via AFOSR/NP on an as–is basis; that is, no guarantee, no warranty, no software support, and no hardware/installation support.

If other equipment is used or if another FORTRAN compiler is used some source code changes will be necessary. For example, Ryan–McFarland Corp. version 1.00 (1984) had several integer and real*4 to real*8 conversion bugs that severely affected results from the air chemistry code for altitudes above 200,000 ft. The difficulty was not in overflow (+++++) or underflow (-----) but in not–a–number (NAN) generation (?????). Version 1.22 and better source code programing have eliminated this problem. The data in Appendix B for helium and air should be duplicated before any modifications to the source code are attempted.

Variable names were chosen to allow easy interpretation of the source code. Comments are included to help simplify code modification. Table C–I is a succinct guide to how the program was organized and manipulated into 64–kB blocks. Three common blocks were coded (as include files) to simplify the exchange of data between subroutines. Coding these common blocks as a matrix and passing them as an explicit variable was initially attempted. This approach eventually produces an error related to the number of variable names in a subroutine call. The large common blocks eliminated that difficulty. The function and its Jacobian had another subroutine limitation: the number of instructions. This was overcome by breaking large subroutines into smaller ones, and then calling them sequentially.

Table C–1
PROGRAM ORGANIZATION

DOS File Name	Subroutine	Common Blocks
AIRA.FOR	– include –	/AIR$MOL/
AIRB.FOR	– include –	/RATES/
AIRC.FOR	– include –	/EXTENT/
AIR.FOR	Main program TABLES$A ENG	– none – /blank common/,/AIR$MOL/ – none –
AIR1.FOR	PHOTO AIR$COMP XRA MOMENTUM F$RATE SET$RATE	/AIR$MOL/ /AIR$MOL/ /AIR$MOL/ /AIR$MOL/ – none – – none – (ENTRY in F$RATE)
AIR2.FOR	A$RATES	/AIR$MOL/,/RATES/
AIR3.FOR	AIR$CHEM	/blank common/,/AIR$MOL/
AIR4.FOR	F$ODE F$YDOT	/AIR$MOL/,/RATES/,/EXTENT/ /AIR$MOL/,/EXTENT/
AIR5.FOR	J$ODE J$A J$B J$C	/AIR$MOL/,/RATES/ /AIR$MOL/,/RATES/ /AIR$MOL/,/RATES/ /AIR$MOL/,/RATES/
AIR6.FOR	J$NEG J$POS CBALANCE	/AIR$MOL/,/RATES/ /AIR$MOL/,/RATES/ – none–
ODE1.FOR	– include –	/AIR$MOL/
ODE2.FOR	– include –	/RATES/
ODE3.FOR	– include –	/EXTENT/

Source code for the air chemistry program is divided into the 13 files described in Table C–1. The description of each program element in Table C–2 will help in any code modification. Modification of this code is complex, even after the operation of LSODE is understood. Addition or reduction of a species involves a change in the number of unknowns, which affects the dimensioning of y, ydot, and pd; subroutines CBALANCE and TABLES$A; the output data matrix; and the AIR$MOL, RATES, and EXTENT common blocks. Adding to or reducing the number of reactions is much simpler, because only y, ydot, pd, A$RATES, and the EXTENT common block are affected.

Programming can be profoundly simplified by using the numerical Jacobian internal to LSODE; however, the execution time of a simulation increases significantly. This possibility is only suggested for operation on a machine that is at least an order of magnitude faster than an early model IBM AT. The explicit Jacobian coding was necessary to reduce the execution time for a simulation by a factor of 50. The data in Appendix B took approximately 5 min per data point.

Auxiliary software on the diskette is noted in Table C–3. The differential equation solver used in this program is LSODE, developed by Hindmarsh [34]. A copy of the support documentation for the Hindmarsh code is provided in ODE0.TXT. The program JACOBIAN checks the coding of the explicit Jacobian. If any changes are made to the number of reactions or the number of species, JACOBIAN should be run to verify complete coding.

JACOBIAN was developed because some simulation data did not seem to make sense. A number of species were continually assuming negative values when there was no physical reason for it. The difficulty was traced back to eight coding errors in 1500 lines of the Jacobian and a common block that was coded differently in one subroutine. The include statements were adopted to eliminate the latter difficulty. LINK$JAC.BAT is an example of how to link all the required subroutines of JACOBIAN.

Because the program contains many lines of code, each of 13 files can be compiled separately to save time. LINK$AIR.BAT is an example of how to link these separate segments into an EXE file.

Table C–2
PROGRAM ELEMENTS

Program Element	Description
Main program	Sequentially calls subroutines to define gas composition, initial conditions, and differential equation solver LSODE
Output FORT70	Written to default disk drive, contains tabular output of simulation identical to the output directed to the screen
Output FORT71	Written to default disk drive, contains numerical simulation data saved in the format of I,AIR$DATA(60) described in AIR$CHEM
/AIR$MOL/	Common block: concentration of gas species
/RATES/	Common block: reaction rates keyed to numbering system in Appendix A
/EXTENT/	Common block: extent of reaction with numbering keyed to reactions in Appendix A
TABLES$A	Subroutine: Output data matrix to screen and to printer via the output file FORT70
ENG	Converts Real*4 numbers to engineering notation
PHOTO	Photoionization data for atmospheric ions and a xenon flashlamp (incomplete)
AIR$COMP	Initializes neutral gas densities for earth's atmosphere, synthetic air, and helium
XRAY	Initializes ionization by product densities data extracted from various references
MOMENTUM	Momentum–transfer collision rate based on gas composition and temperature, Itakawa [18]
F$RATE	Sets parameters that define an ionization pulse: ionization rate, duration, waveform, etc.
SET$RATE	ENTRY in F$RATE for pulsed ionization
A$RATES	Defines reaction rates
AIR$CHEM	Defines Y and AIR$DATA matrices Selects simulation parameters CALL to LSODE solver

Table C-2 (Concluded)

Program Element	Description
F$ODE	Subroutine: contains the extent of reaction and a CALL to F$YDOT that defines the derivatives of the function that LSODE solves F$ODE is defined as an EXTERNAL The name F$ODE is passed in a CALL to LSODE in subroutine AIR$CHEM (AIR3.FOR) F$ODE is passed to LSODE in subroutine AIR$CHEM in AIR3.FOR Y is the species concentration matrix YDOT is the differential equation matrix
F$YDOT	YDOT derivatives related to extent of reaction
J$ODE	Jacobian call by LSODE: method flag 21 User-supplied full Jacobian J$ODE is defined as an EXTERNAL The name J$ODE is passed in a CALL to LSODE in subroutine AIR$CHEM (AIR3.FOR) J$ODE consists of seven segments J$ODE contains part of the neutral species
J$A	Part of J$ODE, neutral species
J$B	Part of J$ODE, neutral species
J$C	Part of J$ODE, neutral species
J$NEG	Part of J$ODE, negative species
J$POS	Part of J$ODE, positive species
CBALANCE	Part of J$ODE, modifies values of Y matrix to maintain charge equilibrium
ODE1	Lawrence Livermore: ordinary differential equation solver (Hindmarsh); documentation, control codes, and error codes on file ODE0.TXT, first of three segments
ODE2	LSODE: second of three segments
ODE3	LSODE: third of three segments

Table C–3
AUXILIARY SOFTWARE

DOS File Name	Description
ODE0.TXT	Documentation for LSODE: control codes, error codes, example program
LINK$AIR.BAT	BAT file to link individual program segments into AIR.EXE
AIR.EXE	EXE file for air–chemistry code
JACOBIAN.FOR	An explicit Jacobian checker to check accuracy
LINK$JAC.BAT	BAT file to link individual program segments into JACOBIAN.EXE
JACOBIAN.EXE	EXE file for JACOBIAN
CCDR.FOR	Cold–Collisional–Dispersion relation versus frequency versus electron density versus collision frequency
CCDR.EXE	EXE file for CCDR
EPSTEIN.FOR	Scattering and absorption by an Epstein profile Generates ASCII file FORT70: reflection coefficient or total return [14] versus frequency
EPSTEIN.EXE	EXE file for EPSTEIN

CCDR is provided as a means of evaluating the cold–collisional–dispersion relation for any frequency, collision rate, and electron number density. It is easy to run and provides tabular listings in file FORT70 of the complex wave number as a function of the above quantities. This program can be run for a single frequency and collision rate with the number density set to vary. The resulting variation in wave number as a function of number density can be interpreted as the effect on wave number of a plane wave incident on an Epstein profile. If $Re(\mathrm{k})$ remains close to its free–space value, the backscatter reflection coefficient is small. If $Im(\mathrm{k})$ increases, the plasma will exhibit some attenuation.

EPSTEIN is a program that computes the reflection or round–trip absorption of a plane wave on an Epstein profile as a function of frequency. It is an implementation of the reflection coefficient and total reduction described in Section IV of Reference 14 (copy attached). This program prompts for reflection or total reduction, collision rate, frequency range, electron number density, and the Epstein profile gradient scale factor. Up to four sets of electron densities and gradient scale factors can be described each time this program is run. The output of EPSTEIN is ASCII file FORT70, which is in a format suitable for most plotting packages.

REFERENCES

[1] R. J. Vidmar, "Generation of Tenuous Plasma Clouds in the Earth's Atmosphere," Annual Report for AFOSR/NP Contract F49620–85–K–0013, SRI International, Menlo Park, CA, pp. 43, 1987.

[2] R. J. Vidmar, "Generation and Properties of Tenuous Plasma Bodies at Atmospheric Pressure," Annual Report for AFOSR/NP Contract F49620–85–K–0013, SRI International, Menlo Park, CA, pp. 35, 1988.

[3] N. D. Borisov and A. V. Gurevich, "High–Frequency Pulsed Air Breakdown in Intersecting Radio Beams," Geomagnetism and Aeronomy, vol. 20, pp. 587–591, 1980.

[4] A. V. Gurevich, "An Ionized Layer in a Gas (in the Atmosphere)," Sov. Phys. Usp., vol. 23, pp. 862–865, 1980.

[5] N. C. Gerson, Radio Wave Absorption in the Ionosphere, New York: Pergamon Press, 1962.

[6] M. Gunar and R. Mennella, "Signature Studies for a Re–Entry System," Proceedings of the Second Space Congress—New Dimensions in Space Technology, Canaveral Council of Technical Societies, pp. 515–548, 1965.

[7] S. Glasstone and P. J. Dolan, The Effects of Nuclear Weapons, Washington: United States Department of Defense and Energy Research and Development Administration, pp. 461–513, 1977.

[8] M. Mitchner and C. Kruger, Partially Ionized Gases, New York: Wiley and Sons, pp. 47–53, 155–162, 1973.

[9] B. Tanenbaum, Plasma Physics, New York: McGraw–Hill, pp. 62–85, 1967.

[10] P. S. Epstein, "Reflection of Waves in an Inhomogeneous Absorbing Medium," Proc. Nat. Acad. Sci., Wash, vol. 16, pp. 627–637, 1930.

[11] K. G. Budden, The Propagation of Radio Waves, Cambridge (Great Britain): Cambridge University Press, pp. 470–475, 550–582, 1985.

[12] W. G. Chesnut, "Radar Reflection Coefficients From a Plasma Gradient With Collisions," Special Report 10, prepared for DASA, Contract DA–49–146–XZ–184, Stanford Research Institute, Menlo Park, CA, October 1968.

[13] C. Lanczos, "A Precision Approximation of the Gamma Function," J. SIAM Numerical Analysis, Ser. B, vol. 1, pp. 86–96, 1964.

[14] R. J. Vidmar, "On the Use of Atmospheric Pressure Plasmas as Electromagnetic Reflectors and Absorbers," submitted to IEEE Plasma Science (copy of submission in attachments), 1990.

[15] Product information bulletins for pyramid and wedge absorbers: Advanced Electromagnetics Inc, Santee, CA; Emerson & Cummings Inc, Gardena, CA; and Rantec Division, Emerson Electric Co., Canoga Park, CA, 1989.

[16] G. T. Ruck et al., Radar Cross Section Handbook, Volumes 1 and 2, New York: Plenum Press, 1970.

[17] E. F. Knott, J. F. Shaeffer, and M. T. Tuley, Radar Cross Section, Dedham, MA: Artech House, 1985.

[18] Y. Itikawa, "Effective Collision Frequency of Electrons in Gases," The Physics of Fluids, vol. 16, pp. 831–835, 1973. (Note: typo in Table II, 10^{-18} should be 10^{-8} $sec^{-1}cm^3$.)

[19] F. R. Attix, Introduction to Radiological Physics and Radiation Dosimetry, New York: Wiley, pp. 160–187, 1986.

[20] R. Deloche, R. P. Monchicourt, M. Cheret, and F. Lambert, "High–Pressure Helium Afterglow at Room Temperature," Physical Review A, vol. 13, pp. 1140–1176, 1976.

[21] M. H. Bortner and T. Bauer, Defense Nuclear Agency Reaction Rate Handbook, 2nd Ed., Santa Barbara, CA: DASIAC, 1972.

[22] M. N. Spencer, J. S. Dickinson, and D. J. Eckstrom, "Afterglow Conductivity Measurements of Air and N_2 Following Intense Electron–Beam Excitation," J. Phys. D: Appl. Phys., vol. 20, pp. 923–932, 1987.

[23] L. M. Biberman, V.S. Vorob'ev, and I. T. Yakubov, Kinetics of Nonequilibrium Low–Temperature Plasmas, New York: Consultants Bureau, 1987.

[24] B. E. Cherrington, Gaseous Electronics and Gas Lasers, Oxford, England: Pergamon Press, 1979.

[25] B. M. Smirnov, Physics of Weakly Ionized Gases, Moscow, USSR: Mir Publishers, 1981.

[26] D. Watters and R. Vidmar, "Inflatable Target Support for RCS Measurement," AMTA Proceedings, 11th Annual Meeting and Symposium, Monterey, CA, pp. 12–15 to 12–19 (copy in attachments), 9–13 October, 1989.

[27] Product information bulletins for UV sources: "Short–Arc Xenon Flashlamps and Power Supplies," publication F1022B–1, EG&G Electro–Optics, Salem, MA, 1988; "New UV Sources," Publication CH–CRB 2001 88–E, ASEA Brown Boveri, CH–5405 Baden, Switzerland, 1988.

[28] B. Eliasson and U. Kogelschatz, "UV Excimer Radiation from Dielectric Barrier Discharges," Appl. Phys. B, vol. 46, pp. 299–303, 1988.

[29] D. F. Anderson, "A Photoionization Detector for the Detection of Xenon Light," IEEE Transactions on Nuclear Sciences, vol. NS–28, pp. 842–848, 1981.

[30] R. T. Rewick, M. L. Schumacher, S. L. Shapiro, T. B. Weber, and M. Cavalli–Sforza, "Tetrakis(dimethylamino)ethylene: Identification of Impurities and Compatibility with Common Metal, Polymer, and Ceramic Laboratory Materials," Analytical Chemistry, vol. 60, pp. 2095–2099, 1988.

[31] R. A. Holroyd, J. M. Preses, C. L. Woody, and R. A. Johnson, "Measurement of the Absorption Length and Absolute Quantum Efficiency of TMAE and TEA from Threshold to 120 nm," Nucl. Instrum. Methods Phys. Res. A (Netherlands), vol. A261, pp. 440–444, 1987.

[32] T. J. Dwyer, J. R. Greig, D. P. Murphy, J. M. Perin, R. E. Pechacek, and M. Raleigh, "On the Feasibility of Using an Atmospheric Discharge Plasma as an RF Antenna," IEEE Antennas and Propagation, vol. AP–32, no. 2, pp. 141–146, 1984.

[33] D. L. Baulch, R. A. Cox, P. J. Crutzen, R. F. Hampson Jr., J. A. Kerr, J. Troe, and R. T. Watson, "Evaluated Kinetic and Photochemical Data for Atmospheric Chemistry: Supplement I," J. Phys. Chem. Ref. Data, vol. 11, no. 2, pp. 327–409, 1982.

[34] A. C. Hindmarsh, "LSODE and LSODI, Two New Initial Value Ordinary Differential Equation Solvers," ACM–Signum Newsletter, vol. 15, no. 4, pp. 10–11, 1980.

ATTACHMENT

REFERENCE 14

R. J. Vidmar, "On the Use of Atmospheric Pressure Plasmas as Electromagnetic Reflectors and Absorbers," submitted to IEEE Plasma Science, 1990.

ON THE USE OF ATMOSPHERIC PRESSURE PLASMAS AS ELECTROMAGNETIC REFLECTORS AND ABSORBERS

Robert J. Vidmar, Member, IEEE

SRI International

Menlo Park, CA 94025

Abstract —— Tenuous plasmas in the earth's atmosphere from sea level to 100 km can be modeled as a cold collisional plasma. If an ionization process results in an electron density profile, such as an Epstein profile, that decreases from a maximum as a function of distance, then the plasma can either reflect or absorb electromagnetic waves, depending on the plasma characteristics. A high reflection coefficient requires a grazing angle of incidence, a low momentum–transfer collision rate, a high plasma density, and a short free–space to plasma transition relative to a wavelength. High absorption from VHF through X–band requires a high collision rate, a low plasma density, and a plasma transition of approximately one wavelength. Both extremes are discussed. Typical collision rates and plasma lifetimes at atmospheric pressure are quantified. Power required to sustain a plasma in air is high because of a short plasma lifetime, but a noble gas contained within a membrane has a longer plasma lifetime and a lower power requirement. Two means of ionization are discussed: high–energy electron–beam impact and UV photoionization of an organic vapor.

Supported by Air Force Office of Scientific Research, AFOSR/NP, contract F49620–85–K–0013.

I. INTRODUCTION

The electromagnetic properties of a plasma at atmospheric pressure is an interdisciplinary topic that combines plasma physics, radio wave propagation, and air chemistry. In this paper, the atmosphere extends from sea level to 100 km (300,000 ft), and the plasma body exists in free space. Prior research on naturally occurring and man–made atmospheric plasma bodies quantifies radio wave effects. Gerson [1] describes D–layer absorption, Gunar and Mennella [2] note fluctuations in radar backscatter as well as the communication blackout of reentry vehicles, and Glasstone and Dolan [3] describe the effects of a nuclear weapon generated plasma on radio and radar signals.

Figure 1 depicts two uses of man–made plasmas. Borisov and Gurevich [4] and Gurevich [5] suggested that crossed high–power electromagnetic pulses could break down air below the D–layer and so form a plasma layer. This layer could be used to reflect signals to a great range, and the highest frequency for reflection would depend on the electron number density in the slab. A plasma could also be used as an absorber, as illustrated in Fig. 1(b). The absorption, power required, and bandwidth are described in this paper.

These man–made plasmas each use an ionization source to generate a tenuous plasma, resulting in an electron number density, n_e, that is high near the source and diminishes with distance from the source. After the source shuts off, n_e decreases as a function of time as electrons recombine with positive ions or attach to form negative ions. Section II describes the electromagnetic properties that are essential to an understanding of these man–made plasmas. The theory model for scattering parameters is derived from the work of Epstein [6] as presented by Budden [7] in the context of

scattering from plasma gradients in the ionosphere. Electromagnetic properties, such as wave number, power reflection coefficient, and absorption coefficient, are a function of the host gas and plasma.

Section III presents gas and plasma characteristics, such as momentum–transfer collision rate, plasma lifetime, recombination kinetics, and the effect of noble gases. For example, a noble gas, used instead of air as a host gas, extends the plasma lifetime by reducing negative–ion formation. Several tables and figures quantify a wide range of values used to estimate the performance and power required to sustain a plasma.

Applications for a plasma with a gradient, discussed in Section IV, include (a) a high–altitude plasma that can reflect or absorb from HF to VHF, and (b) a broadband atmospheric pressure absorber. A novel characteristic of plasma used as an absorber is its bandwidth that extends from VHF through X–band at atmospheric pressure.

Section V describes the generation and use of plasma, including electron impact ionization with a high–energy electron–beam source and UV photoionization of an alkali vapor or an organic vapor, such as tetrakis(dimethylamino)ethylene, TMAE, [8]–[10]. The power required to sustain a plasma is quantified, and properties such as maximum absorption and bandwidth are discussed. Trade–offs among maximum absorption, absorption bandwidth, duty ratio, and applied power permit optimization of absorption primarily at VHF.

II. ELECTROMAGNETIC CHARACTERISTICS

A. Cold Collisional Plasma

In an atmospheric pressure plasma, electrons undergo numerous collisions with atoms and molecules in the neutral background gas. Collisions damp electron motion and so convert electromagnetic energy coupled into electron motion directly to heat. Electrons produced by an ionization source cool rapidly in collisions with the background gas. The host gas (air or a noble gas confined by a membrane) is at the ambient atmospheric temperature and under many circumstances has sufficient heat capacity to cool electrons with little change in temperature.

If the ionization process maintains an electron temperature above 1 eV, then a multi–specie full–kinetic model is necessary because of electronic excitation, dissociation, ionization, an so on. Whenever host gas heating due to generation of a tenuous plasma body is negligible, then the electron temperature is near the ambient temperature. After hot electrons cool to a fraction of an eV, plasma characteristics can be approximated via a cold collisional plasma model [11], [12].

The dispersion relation for a cold collisional plasma with a constant momentum–transfer collision rate, ν, is

$$k(\omega) = \frac{\omega}{c}\left[1 - \frac{\omega_p^2}{\omega(\omega - i\nu)}\right]^{1/2} \tag{1}$$

where k is a complex wave number, ω is angular frequency, $i = \sqrt{-1}$, and c is the speed of light. The plasma angular frequency is $\omega_p = (n_e e^2/m_e \epsilon_o)^{1/2}$, where e and m_e are the electron charge and mass, n_e is the electron number density, and ϵ_o is the free–space permittivity.

The wave number is $k = k_r + ik_i$, where $k_r = Re(k)$ and $k_i = Im(k)$. Wave motion is proportional to $\exp[+i(\omega t - k_r z)] \exp(+k_i z)$, where z is propagation distance and k_i is the attenuation constant. A lossless plasma ($\nu = 0$) exhibits a wave propagation cutoff for $\omega \leq \omega_p$. A collisional plasma with $n_e = 2 \times 10^{11}$ cm^{-3} and $\nu = 300 \times 10^9$ s^{-1} has $\omega_p = 25 \times 10^9$ s^{-1}, a conductivity similar to sea water, and a wave number that remains finite for $\omega < \omega_p$. The value of k at 1 GHz is $k_r = 20.96$ m^{-1} and $k_i = -3.475$ m^{-1}.

For $\omega < \nu$ and $\omega < \omega_p^2/\nu$, k_r and k_i simplify to $k_r \simeq \omega/c$ and $k_i \simeq -\omega_p^2/(2\nu c)$. Absorption to first order is broadband in nature and independent of frequency below ω_p^2/ν. But, the transition from free space to plasma produces a reflection that is frequency dependent. The magnitude of the reflection depends on the spatial distribution of plasma in the transition region.

B. Epstein Profile Model

An Epstein profile provides an analytical model for estimating scattering coefficients from plasmas that have a smooth electron density gradient [6], [7]. An Epstein electron number–density profile is

$$n(z) = \frac{n_o}{1 + \exp(-z/\sigma)} \tag{2}$$

where n_o is the electron density at $z = +\infty$, σ is a gradient scale factor, and ν is independent of z. A plane wave propagating from $z = -\infty$ to $z = +\infty$ encounters an increasing electron number density that results in a reflection determined by the gradient scale factor, σ, and n_o.

C. Power Reflection and Transmission Coefficients

The power reflection and transmission coefficients for a wave incident at angle θ on an Epstein profile are described by Budden [7, Chapter 11]

$$R = \left|\frac{C - q}{C + q}\right|^2 \left|\frac{\Gamma[1 + ik\sigma(q + C)]}{\Gamma[1 + ik\sigma(q - C)]}\right|^4 \tag{3}$$

$$T = \frac{|Cq|}{|C + q|^2} \left|\frac{\Gamma^2[1 + ik\sigma(q + C)]}{\Gamma[1 + 2ik\sigma q]\Gamma[1 + 2ik\sigma C]}\right|^2 \exp[+2Im(q)z] \tag{4}$$

$$q^2 = C^2 - \frac{\omega_p^2}{\omega(\omega - i\nu)} \tag{5}$$

where k is the free–space wave number, $C = \cos(\theta)$, and q is a solution of the Booker quartic described in [7].

The second term of q^2 in (5) has a magnitude much less than unity at high frequency, $\omega > \omega_p$ and $\omega > \nu$, but is large and primarily complex for $\omega < \omega_p$ and $\omega < \nu$. Before resorting to the machine calculations of (3) and (4) in Section IV, consider three limiting cases.

For $\sigma \to 0$, an Epstein profile approximates a slab discontinuity at $z = 0$. The arguments of the gamma functions in (3) and (4) equal unity, and the values of R and T reduce to the Fresnel reflection formulas [7].

The second case is for grazing angle illumination, $\theta \to 90°$ so that $C \to 0$. The arguments of the gamma functions in (3) and (4) then approach unity for any σ and ν. The reflection coefficient approaches unity, and the transmission coefficient approaches zero. This suggests the use of a tenuous plasma as a reflector at a grazing angle.

The third case is for $\theta = 0$, the backscatter reflection coefficient. In (3) the argument of the gamma function in the numerator is + 2ikσ larger than that in the denominator. Using Euler's formula, the absolute value for the ratio of gamma functions is

$$\left|\frac{\Gamma(z + 2ik\sigma)}{\Gamma(z)}\right| = \lim_{n\to\infty} \left|\frac{z}{(z+iy)}\right|^4 \left|\frac{(z+1)}{(z+iy+1)}\right|^4 \cdots \left|\frac{(z+n)}{(z+iy+n)}\right|^4 \qquad (6)$$

where $y = 2k\sigma$ and $z = 1 + ik\sigma(q-1)$. For $\omega < \omega_p$ and $\omega < \nu$, the value of q reduces to $q \simeq C - i\omega_p^2/(2\omega\nu C)$ or $q - 1 = -i\omega_p^2/(2\omega\nu)$ for $\theta = 0$. For any value of $\sigma > 0$, z is real and y is imaginary. Therefore each term in the infinite product maintains $|(z+n)/(z+iy+n)|^4 \leq 1$ and the value of (6) is less than one.

Because R is the product of the Fresnel reflection coefficient and (6), reflection from an Epstein profile varies with frequency and slab thickness. For $\omega \ll \omega_p^2/(4\nu)$, the wavelength is much longer than the slab dimension, $z \gg y$, the value of (6) is approximately one, and the reflection coefficient reduces to the Fresnel term. For $\omega = \omega_p^2/(4\nu)$ and $\sigma = \lambda/(4\pi)$, y =1, z = 2, and the first few terms are proportional to $(4/5)^2$. At a higher frequency such that $\omega = \omega_p^2/\nu$ and $\sigma = \lambda/4$, $y = \pi$, $z = 1 + \pi/4$, and the first few terms are proportional to $\sim(1/4)^2$. Hence, the reflection coefficient for backscatter can become small. A small reflection coefficient results from incoherent backscatter from the plasma gradient rather than a coherent reflection at a slab discontinuity.

D. Attenuation Coefficient

In addition to scattering fro. the plasma, a signal that propagates into an Epstein gradient and then reflects from a good conductor will have its field quantities reduced by $\exp(-2\int k_i dz)$, where the integral is from $z = -\infty$ to the surface of the conductor at $+z_0$. The factor of 2 in the exponential denotes a round trip. For a tenuous plasma, k_i is proportional to n_e integrated over all space. The integral of an Epstein profile from $-z_0$ to $+z_0$ is $n_0 z_0$. The round-trip attenuation in dB for a plasma with $\omega < \nu$ and $\omega < \omega_p^2/\nu$ is

$$A(dB) = 4.343 \left[\frac{e^2 h}{\epsilon_0 m_e c}\right] \left[\frac{n_e}{\nu}\right] \tag{7}$$

where h $(=2z_0)$ is the total thickness of the plasma and n_e is in m^{-3}. The 5% and 95% values of n(z) for an Epstein profile correspond to $\mp z_0 = 2.944\sigma$, respectively. For an Epstein profile spanning the 5% to 95% range, h is 5.888σ, and attenuation is $A(dB) = 2.71 \times 10^{-4}\, n_e \sigma/\nu$.

E. Numerical Evaluation

To evaluate the reflection and transmission coefficients in (3) and (4), the gamma function $\Gamma(z)$ for complex arguments in the right-half complex plane must be evaluated. Lanczos [13] developed an asymptotic expansion correct to better than 0.1% for the right-half complex plane. His formula is

$$\Gamma(z+1) = (z+2)^{(z+1/2)}\, e^{-(z+2)}\, (2\pi)^{1/2} \left[0.999779 + \frac{1.084635}{z+1}\right] \tag{8}$$

Because the magnitude of z can become large in (3) and (4), computing $\ln[\Gamma(z+1)]$ prevents an overflow condition and retains accuracy.

III. PLASMA CHARACTERISTICS

A. Momentum–Transfer Collision Rate

The electron momentum–transfer collision rate, ν, is a function of temperature and gas species and sets the value of k_i that determines electromagnetic absorption. Itikawa [14] discusses effective values of ν for atmospheric gases and noble gases over the electron temperature range of 100°K to 5000°K; the data in Table I spans 300°K to 1000°K. In air, 20,000 collisions vill reduce the electron energy by a factor of 40 [11]. pressure of 760 torr (sea level) this process requires 50 ns, based on the 1000°K rate. If thermalization is faster than or comparable to a plasma lifetime, then an effective electron temperature during the afterglow is near the ambient temperature of the host gas.

TABLE I

MOMENTUM–TRANSFER COLLISION RATE

Gas Species	ν/N $\left[10^{-8}\ cm^3 s^{-1}\right]$		
	T_e = 300°K	500°K	1000°K
N_2	0.594	0.959	1.77
O_2	0.286	0.437	0.804
CO_2	10.05	9.68	7.48
H_2O	77.90	56.25	34.6
He	0.763	1.01	1.50
Ne	0.076	0.118	0.217
Ar	0.220	0.146	0.094
Kr	1.775	1.315	0.713
Xe	5.29	3.81	1.90
Dry Air	0.529	0.845	1.550

Data: N is gas density in cm^{-3}

At a pressure of 760 torr and an electron temperature of 500° K, the collision rates for dry air and helium are 212×10^9 s^{-1} and 253×10^9 s^{-1}. Water vapor strongly influences the collision rate at low altitudes. For example, 50% relative humidity increases the sea-level dry-air collision rate from 212×10^9 s^{-1} to 417×10^9 s^{-1}. The values of ν in Table II include the variation of air composition with altitude from sea level to 300,000 ft (91.5 km).

TABLE II

COLLISION RATE IN AIR

Altitude (kft)	Pressure (torr)	Momentum Transfer, Collisions per sec		
		T_e = 300° K	500° K	1000° K
0	760	466×10^9	417×10^9	425×10^9
11.3	500	103	121	180
32.8	200	23.6	37.6	72.0
47.5	100	12.1	19.3	37.1
62.0	50	6.07	9.70	18.6
81.4	20	2.38	3.80	7.27
96.4	10	1.18	1.87	3.57
111.6	5	0.584	0.914	1.73
133.4	2	0.272	0.382	0.672
150.5	1	0.215	0.248	0.365
169.1	500×10^{-3}	122×10^6	134×10^6	189×10^6
192.4	200	26.7	37.8	67.1
209.8	100	11.8	18.3	34.4
225.5	50	5.92	9.42	18.0
245.1	20	2.49	3.98	7.64
253.7	10	1.27	2.03	3.89
274.1	5	0.662	1.06	2.03
291.1	2	0.257	0.411	0.789
300.0	1.32	0.161	0.258	0.494

B. Plasma Lifetime

The plasma lifetime, τ, is the time required for a plasma of initial density n_0 to decrease in concentration by *a factor of 1/e*. It is useful in estimating the power required to sustain a plasma. Estimates of τ have been computed with an air chemistry code developed to model the deionization process [15], [16]. This code takes into account the major atmospheric gases plus H_2O as a function of altitude. The same code has an option to treat helium as the major species with air as an impurity.

The Earth's Atmosphere: The plasma lifetime in air exhibits a dependence on electron number density and on pressure (altitude) as shown in Fig. 1. For $n_e < 10^{12}$ cm^{-3}, three–body attachment to oxygen dominates the deionization process. The slope of the diagonal line in Fig. 2 is due to the decrease in oxygen concentration as a function of altitude. Because the three–body attachment is proportional to the square of the oxygen concentration, plasma lifetime increases by two orders of magnitude for each factor of 10 decrease in atmospheric pressure.

As the concentration of oxygen diminishes with increasing altitude, two–body attachment and recombination processes begin to dominate three–body attachment to oxygen. These processes include dissociative attachment with oxygen and ozone, and dissociative recombination with positive ions. Because attachment depends on the concentration of oxygen and ozone but recombination does not, recombination with positive ions is the dominant loss mechanism at high altitude. Consequently, the plasma lifetime eventually becomes height independent, which results in the horizontal curves in Fig 1.

For $n_e > 10^{12}$ cm^{-3}, dissociative attachment of electrons with positive ions and then three–body electron–electron attachment to positive ions dominate the deionization process. The nearly horizontal curves in Fig. 2 and

the progressively larger separation between curves indicate that three–body attachment (proportional to n_e^2) is starting to dominate for $n_e > 10^{14}$ cm^{-3}. The curves in Fig. 2 were truncated at an altitude for which the energy required for ionization would increase the ambient air temperature by 50°K. For $n_e \leq 10^{12}$ cm^{-3} the amount of heating below 200,000 ft is negligible.

Noble Gases: Significantly longer lifetimes are possible with helium. Helium does not form negative ions, so a major electron attachment mechanism is minimized. Because high purity helium is expensive and impurities always leak into a large vessel, helium with trace amounts of air is the most likely gas mixture. Nitrogen and oxygen impurities rapidly form positive ions in charge transfer collisions with helium ions and in turn recombine with electrons and so deionize the helium plasma.

Simulations of plasma lifetime in helium with 1–ppm, 10–ppm, and 100–ppm air demonstrate lifetimes orders of magnitude longer than air plasma lifetimes, as shown in Figs. 3, 4, and 5, respectively. For $n_e \simeq 10^{11}$ cm^{-3} and impurity concentrations below 100 ppm, the lifetime in helium is ~10^4 times longer than an air plasma at sea level. At an altitude of 100,000 ft (30.5 km, 8.5 torr), air and helium plasmas have similar lifetimes. For a high–purity helium plasma, Deloche [17] observed plasma lifetimes longer than those estimated in Fig. 3.

An engineering estimate for τ in a noble gas is obtained by examining the recombination kinetics to determine if there is a limiting reaction. For $n_e \leq 10^{12}$ cm^{-3} in a noble gas with a trace of air, two–body dissociative recombination is likely to characterize the overall recombination rate, and the plasma lifetime reduces to $\tau = 1/(kn_e)$, where k is a two–body rate constant. Because dimer formation and charge transfer are fast compared to dissociative recombination, the dominant ion for recombination depends on the purity of

the noble gas. Charge transfer resulting in N_2^+ and O_2^+ will increase the rate of recombination by a factor of 10 compared to He_2^+. Two–body rate constants for noble gases and air [18] are shown in Table III.

TABLE III

DISSOCIATIVE RECOMBINATION

Reaction	Rate constant (cm^3/s)
$He_2^+ + e \rightarrow He + He$	1.0×10^{-8}
$Ne_2^+ + e \rightarrow Ne + Ne$	1.8×10^{-7}
$Ar_2^+ + e \rightarrow Ar + Ar$	9.1×10^{-7}
$Kr_2^+ + e \rightarrow Kr + Kr$	1.6×10^{-6}
$Xe_2^+ + e \rightarrow Xe + Xe$	2.7×10^{-6}
$N_2^+ + e \rightarrow N + N$	3.5×10^{-7}
$O_2^+ + e \rightarrow O + O$	1.9×10^{-7}

Data: Temperature = 300°K, 1 $cm^3/s = 10^{-6}$ m^3/s

IV. APPLICATIONS

Figure 1 sketches the use of plasma as a reflector (artificial ionospheric mirror) and as an absorber. If the high–power pulses of [4] and [5] result in the formation of a plasma patch, will the patch reflect or transmit RF? If RF breakdown results in a plasma with a rapid transition from free space to plasma, $\sigma/\lambda \ll 1$, the plasma will reflect. Or, if the transition is diffuse, the plasma will reflect at a grazing angle. If the plasma gradient is too long, that is, $\sigma > \lambda/(4\pi)$, then it will transmit more RF than it reflects.

As an example of an ionospheric mirror, consider a plasma at an altitude of 230,000 ft (70.1 km), a pressure of 40 mtorr, an incident angle of 75 degrees off broadside, and $\nu = 7.4 \times 10^6$ s^{-1}. The curves in Fig. 6 quantify the dependence of the reflection coefficient on σ, the plasma to free-space transition, and on frequency. The value of $n_0 = 10^7$ cm^{-3} was chosen so as to achieve a high reflection coefficient at a sharp boundary for frequencies up to 100 MHz. Note the transition from a good reflector to a poor reflector as the gradient varies from sharp, $\sigma = 10$ cm, to diffuse, $\sigma = 100$ m. Increasing n_0 increases the maximum frequency for high reflectivity. Lowering the altitude increases absorption due to collisions, decreases plasma lifetime, and so requires more power.

As an example of a broadband absorber, consider a plasma in air at sea level with $\nu = 417 \times 10^9$ s^{-1} and $n_0\sigma = 6 \times 10^{10}$ cm^{-3}m. These values were selected to yield a maximum round-trip absorption of 40 dB in Fig. 7. Round-trip absorption refers to the sum of reflection from the gradient (3) plus absorption (8) due to propagating ($h = 5.888\sigma$) into the plasma and reflecting. Doubling n_e will double absorption (7).

Absorption bandwidth depends on the collision rate and the plasma gradient. The high-frequency cutoff is set by ν and has a value of $\sim\nu/5$. The variation of absorption with σ in Fig. 7 indicates that high absorption at a low frequency requires a free-space transition of $4\sigma \simeq \lambda$, that is, one or two wavelengths. The low-frequency cutoff is $\sim c/(4\sigma)$.

A plasma with $\sigma > \lambda/(4\pi)$ and sufficient electron number density has the characteristics of a broadband absorber. This plasma absorber is lightweight, exhibits high attenuation per wavelength, has a broad bandwidth, and can be switched on and off. These characteristics provide a means to control electromagnetic scattering. A plasma at atmospheric pressure could be

used as an absorber for antenna pattern and backscatter measurements; modify the radiation pattern of an antenna; act as a high–power waveguide switch or crowbar; and reduce edge diffraction. Although these applications are predicted and experimental evidence exists to verify the reflective/absorptive characteristics of a collisional plasma, an efficient means of generating a collisional plasma is still evolving.

IV. PRODUCTION AND USE OF PLASMA

A. Plasma Generation

Two requirements of plasma generation for an absorber are that (1) n_e is sufficiently high near the source, and (2) n_e diminishes as a function of distance away from the source. A variety of sources fulfill these requirements. Electron–beam impact ionization and photoionization of a seed molecule are two of many laboratory techniques.

A high–energy (100 keV to 600 keV) pulsed electron beam can generate a plasma in air or noble gases. As electrons emerge from a source, they diverge and interact with matter. The spatial distribution is complex [19] and involves electron backscatter, secondary electron generation, and multiple shallow–angle scattering. These effects provide a mechanism for electrons to curve around and fill in regions not directly illuminated by the beam.

Electron density from a point source falls off as $1/r^2$, and electrons have a maximum range due to their interactions with matter. Because of this continual interaction, electron energy decreases with range. Below 20 keV, the rate of energy deposition increases significantly. This increase results in a

small increase in n_e near its maximum range. High–energy electron–beam sources are commercially available and have been used in laboratory experiments.

Another ionization technique is photoionization of a seed gas such as an alkali or organic vapor. For efficient photoionization, the medium must be optically thick. To achieve the required alkali vapor density for a 1– to 4–meter optical thickness, it must be heated and contained in a membrane not affected by the heat or vapor. An alternative is to use a readily ionized organic vapor with a high vapor pressure such as TMAE. Rewick [10] has identified a number of common materials that could contain TMAE vapor. There are several commercial UV flash lamps, rich below 200 nm, that could readily photoionize TMAE vapor. A plasma generated via photoionization would have a $1/r^2$ distribution that is also attenuated because of the optical range of the medium.

B. Power Estimation

An approximation for the power per unit volume required to sustain a plasma is $P/V = (n_e E_i)/\tau$, where P is the continuous–wave (CW) power (deposited in the plasma), V is the plasma volume, n_e is the electron–plasma density, E_i is the energy to generate an electron–ion pair, and τ is the plasma lifetime (Section III B). For a plasma generated by electron–beam impact, the value of E_i is 41.5 eV for He, 36.2 eV for Ne, 26.2 eV for Ar, 24.3 eV for Kr, 21.9 eV for Xe, 34.6 eV for N_2, 31.8 eV for O_2, and 33.7 eV for dry air. If photoionization of a seed molecule like TMAE is the means of ionization, then E_i is approximately 7 eV.

Consider two examples in air: a plasma absorber at sea level and an ionospheric mirror. For a plasma with $n_e = 10^{11}$ cm^{-3} at 760 torr, the plasma lifetime is 10 ns, and P/V is 54 MW/m^3 for impact ionization. An ionospheric mirror at 230,000 ft (70.1 km) with $n_e = 10^7$ cm^{-3} and $\tau = 800$ ms has a power requirement of 68 μW/m^3 delivered to the plasma. Plasma lifetimes in a noble gas at 760 torr are orders of magnitude longer than in air, which significantly reduces the power requirement.

The power per unit volume for a noble-gas plasma dominated by two-body recombination reduces to

$$\frac{P}{V} = k\, n_e^2\, E_i \tag{9}$$

The rate constants for noble gases are shown in Table III. The rate constant for dissociative recombination of organic vapor ions like $TMAE^+$ have not been measured but are estimated to be of the order of Xe_2^+ in Table III. The power estimates in Table IV are for impact ionization of helium ($E_i \simeq 42$ eV) and photoionization of organic vapors ($E_i \simeq 7$ eV).

C. Use as Absorber

Even though none of the ionization sources mentioned above generates an Epstein profile, the σ parameter in (2) can be adjusted to approximate other distributions. The value of σ is set to match the 5% and 95% values of electron density produced by the ionization source. By making this adjustment, an Epstein profile can be used to estimate electromagnetic effects. The alternative is to use the exact electron distribution and a computational model for scattering from a plasma gradient [7]. An Epstein profile provides a simple first estimate.

TABLE IV

POWER REQUIRED TO SUSTAIN A PLASMA

Plasma Density (cm^{-3})	Power per Unit Volume (W/m^3)		
	$k = 10^{-8}$ cm^3/s $E_i = 42$ eV	10^{-7} cm^3/s 7 eV	10^{-6} cm^3/s 7 eV
10^6	70×10^{-9}	100×10^{-9}	1×10^{-6}
10^7	7×10^{-6}	10×10^{-6}	100×10^{-6}
10^8	700×10^{-6}	1×10^{-3}	10×10^{-3}
10^9	70×10^{-3}	100×10^{-3}	1
10^{10}	7	10	100
10^{11}	700	1×10^3	10×10^3
10^{12}	70×10^3	100×10^3	1×10^6

The data in Table IV has been recast in Table V to provide an estimate of power per unit area as a function of absorption, bandwidth, and gas composition. Bandwidth was deduced from several plots like Fig. 8, for which the collision rate was reduced from that of air at sea level to that of helium and neon/argon at 760 torr. Parameters that yield predictions of attenuation up to 100 dB are noted in Fig. 8. For values of absorption beyond 100 dB backscatter from local inhomogeneities in the plasma gradient adds to round-trip absorption at low frequencies. Predictions of round-trip absorption in excess of 100 dB must take these local inhomogeneities into account.

TABLE V

POWER REQUIRED FOR VHF TO S-BAND ABSORPTION

Absorption (dB)	Power† (W/m^2)		Bandwidth (MHz)	
	Helium	Neon/Argon	Helium	Neon/Argon
40	13,500	180	80 – 10,000	70 – 1,500
60	30,400	420	100 – 9,000	100 – 1,400
80	54,000	780	120 – 6,000	120 – 1,000
100	77,780	1,058	150 – 6,000	150 – 900

† Power refers to CW power per square meter, for a plasma with a 4–m thick plasma that approximates an Epstein profile.

Note the trade–off in Table V between power and bandwidth for a neon/argon–based plasma compared to helium. The high–frequency cutoff is proportional to ν; power is proportional to n_e^2; and absorption (7) is proportional to (n_e/ν). Because the value of ν in neon/argon is approximately a factor of 10 less than helium, the value of n_e in neon/argon is a factor of 10 less than in helium for the *same* absorption,. This reduces bandwidth by a factor of 10, but power decreases by a factor of 100.

The power in Tables IV and V is the power deposited in the plasma and so does not account for source efficiency. Generating plasma intermittently with a low duty ratio is one way to produce a large volume of plasma absorber with simple equipment. Other more efficient means of ionization could increase the duty ratio or permit the use of gases that demonstrate a broader bandwidth.

V. CONCLUSION

The theory, experimental evidence, and calculations support use of plasmas at atmospheric pressure as reflective/absorptive media. Electromagnetic characteristics were evaluated with an Epstein profile model that can be used to approximate the electron distributions generated by an ionization source. Although the modeling of the source distribution function is approximate, the Epstein profile model provides a simple estimate of electromagnetic absorption and scattering.

Plasma generated in air or helium at atmospheric pressure has the novel property of being an excellent broadband absorber from VHF to X–band. The power required to sustain a plasma in a noble gas like helium is orders of magnitude less than in air, because noble gases do not form negative ions. A neon/argon plasma has the property of high absorption from VHF to S–band and requires less power to sustain than a helium plasma, because its momentum–transfer collision rate is lower.

These characteristics suggest that plasmas at atmospheric pressure have the potential of becoming a useful engineering material from VHF to X–band. The gap in knowledge to this practical end involves a better understanding of scattering parameters, ionization and recombination gas kinetics, and efficient ionization techniques.

ACKNOWLEDGMENT

This work was supported by Air Force Office of Scientific Research, AFOSR/NP, contract F49620–85–K–0013. The author acknowledges many productive discussions with D. Eckstrom and W. Chestnut.

REFERENCES

[1] N. C. Gerson, Radio Wave Absorption in the Ionosphere, New York: Pergamon Press, 1962.

[2] M. Gunar and R. Mennella, "Signature Studies for a Re-Entry System," Proceedings of the Second Space Congress—New Dimensions in Space Technology, Canaveral Council of Technical Societies, pp. 515–548, 1965.

[3] S. Glasstone and P. J. Dolan, The Effects of Nuclear Weapons, Washington: United States Department of Defense and Energy Research and Development Administration, pp. 461–513, 1977.

[4] N. D. Borisov and A. V. Gurevich, "High-Frequency Pulsed Air Breakdown in Intersecting Radio Beams," Geomagnetism and Aeronomy, vol. 20, pp. 587–591, 1980.

[5] A. V. Gurevich, "An Ionized Layer in a Gas (in the Atmosphere)," Sov. Phys. Usp., vol. 23, pp. 862–865, 1980.

[6] P. S. Epstein, "Reflection of Waves in an Inhomogeneous Absorbing Medium," Proc. Nat. Acad. Sci., Wash, vol. 16, pp. 627–637, 1930.

[7] K. G. Budden, The Propagation of Radio Waves, Cambridge (Great Britain), Cambridge University Press, pp. 470–475, 550–582, 1985.

[8] D. F. Anderson, "A Photoionization Detector for the Detection of Xenon Light," IEEE Transactions on Nuclear Sciences, vol. NS–28, pp. 842–848, 1981.

[9] R. A. Holroyd, J. M. Preses, C. L. Woody, and R. A. Johnson, "Measurement of the Absorption Length and Absolute Quantum Efficiency of TMAE and TEA from Threshold to 120 nm," Nucl. Instrum. Methods Phys. Res. A (Netherlands), vol. A261, pp. 440–444, 1987.

[10] R. T. Rewick, M. L. Schumacher, S. L. Shapiro, T. B. Weber, and M. Cavalli–Sforza, "Tetrakis(dimethylamino)ethylene: Identification of Impurities and Compatibility with Common Metal, Polymer, and Ceramic Laboratory Materials," Analytical Chemistry, vol. 60, pp. 2095–2099, 1988.

[11] M. Mitchner and C. Kruger, Partially Ionized Gases, New York: Wiley and Sons, pp. 47–53, 155–162, 1973.

[12] B. Tanenbaum, Plasma Physics, New York: McGraw–Hill, pp. 62–85, 1967.

[13] C. Lanczos, "A Precision Approximation of the Gamma Function," J. SIAM Numerical Analysis, Ser. B, vol. 1, pp. 86–96, 1964.

[14] Y. Itikawa, "Effective Collision Frequency of Electrons in Gases," (Note, typo in Table II, 10^{-18} should be 10^{-8} $sec^{-1}cm^3$), The Physics of Fluids, vol. 16, pp. 831–835, 1973.

[15] R. J. Vidmar, "Generation of Tenuous Plasma Clouds in the Earth's Atmosphere," Annual Report for AFOSR/NP contract F49620–85–K–0013, SRI International, Menlo Park, CA, pp. 43, 1987.

[16] R. J. Vidmar, "Generation and Properties of Tenuous Plasma Bodies at Atmospheric Pressure," SRI Annual Report for AFOSR/NP contract F49620–85–K–0013, SRI International, Menlo Park, CA, pp. 35, 1988.

[17] R. Delcche, R. P. Monchicourt, M. Cheret, and F. Lambert, "High–Pressure Helium Afterglow at Room Temperature," Physical Review A, vol. 13, pp. 1140–1176, 1976.

[18] L. G. Christophorou, Electron–Molecule Interactions and Their Applications, Volume 2, Orlando: Academic Press, pp. 74–77, 1984.

[19] F. R. Attix, Introduction to Radiological Physics and Radiation Dosimetry, New York: Wiley, pp. 160–187, 1986.

FIGURE CAPTIONS

Fig. 1. Plasma at atmospheric pressure used (a) as a reflector and (b) as an absorber.

Fig. 2. Plasma lifetime of air versus altitude.

Fig. 3. Plasma lifetime of helium with 1 ppm air.

Fig. 4. Plasma lifetime of helium with 10 ppm air.

Fig. 5. Plasma lifetime of helium with 100 ppm air.

Fig. 6. Reflection from an Epstein profile at 230,000 ft (70.1 km).

Fig. 7. Absorption plus reflection from an Epstein profile in air at 760 torr.

Fig. 8. Absorption plus reflection from an Epstein profile in helium and neon/argon at 760 torr.

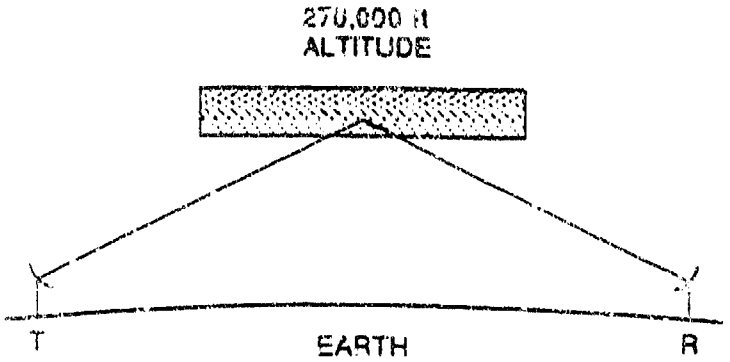

(a) SIGNAL REFLECTS FROM PLASMA WITH STEEP GRADIENT AT GRAZING ANGLE

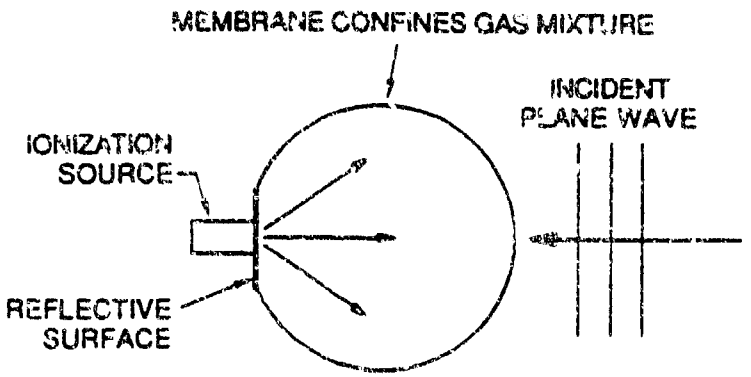

(b) SOURCE IONIZES NOBLE GAS SEED-GAS MIXTURE AND GENERATES PLASMA GRADIENT

RML 362-8556-7

FIGURE 1 PLASMA AT ATMOSPHERIC PRESSURE USED (a) AS A REFLECTOR AND (b) AS AN ABSORBER

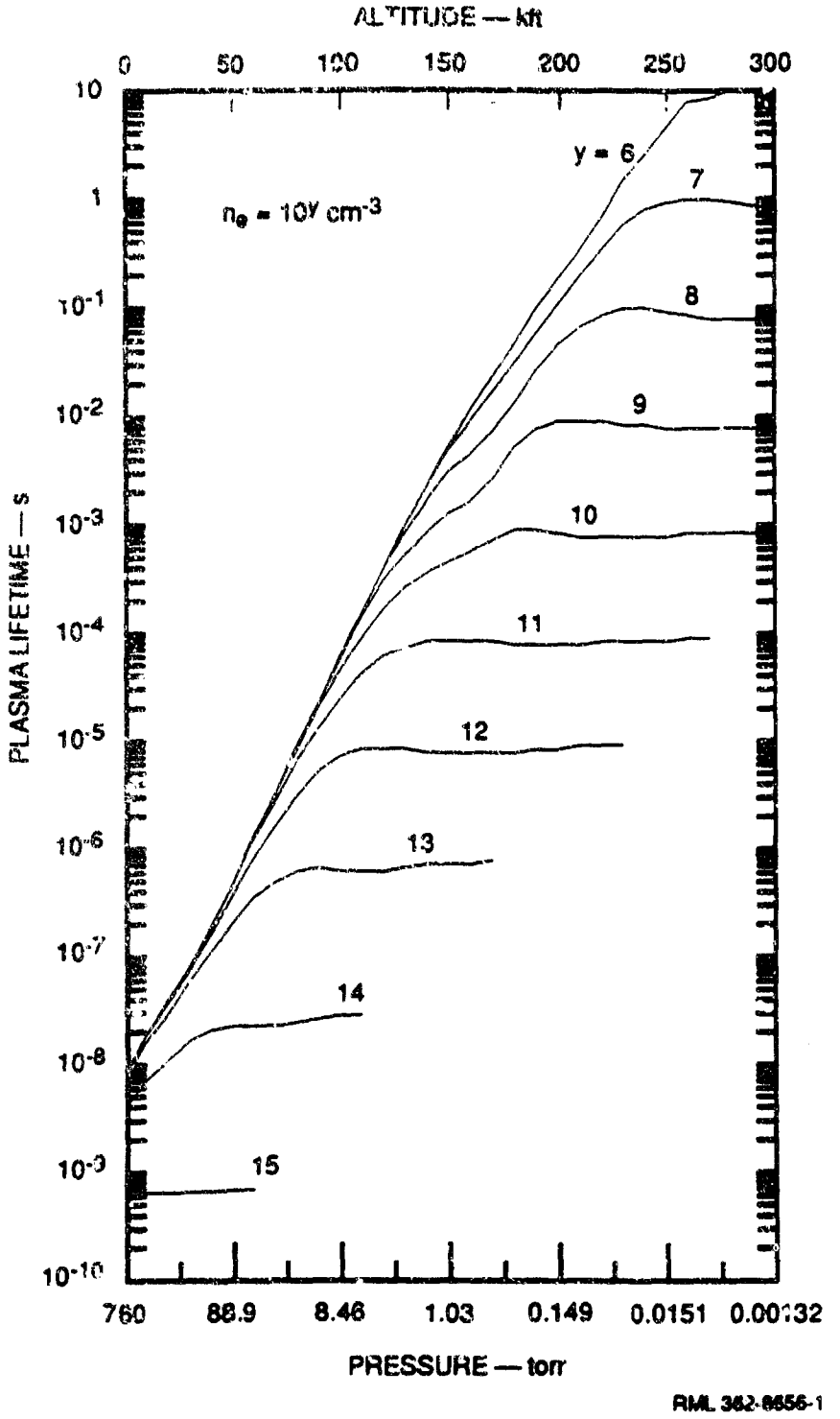

FIGURE 2 PLASMA LIFETIME OF AIR VERSUS ALTITUDE

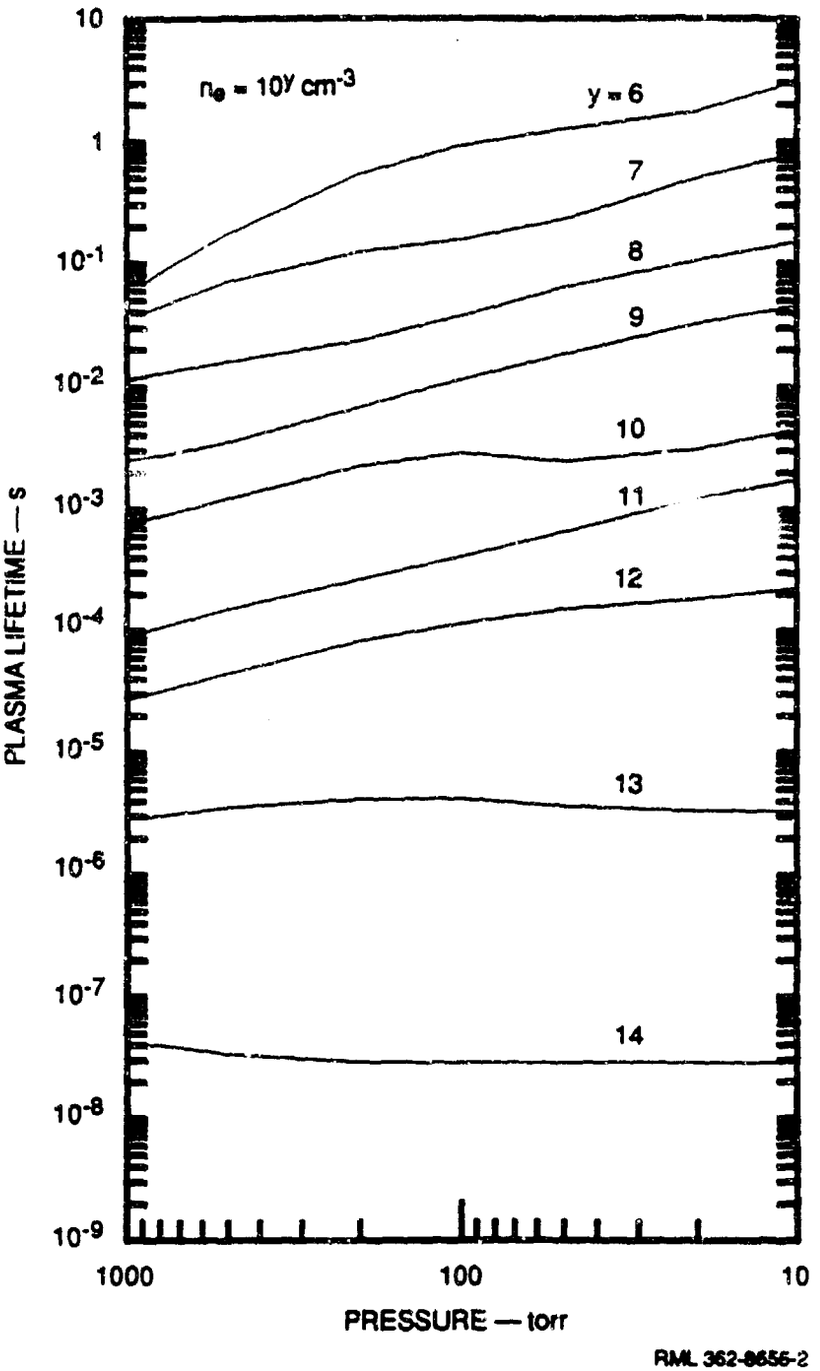

FIGURE 3 PLASMA LIFETIME OF HELIUM WITH 1 ppm AIR

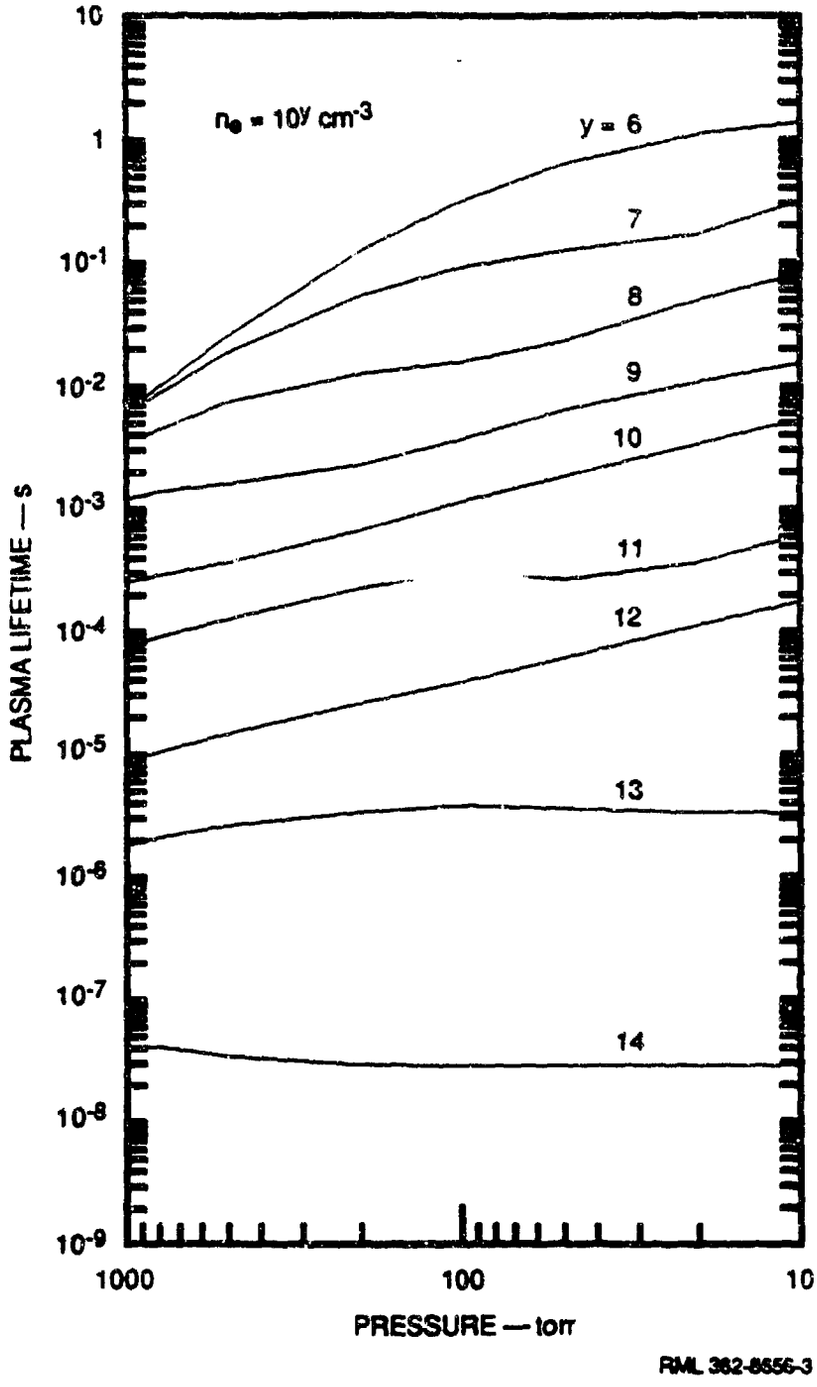

FIGURE 4 PLASMA LIFETIME OF HELIUM WITH 10 ppm AIR

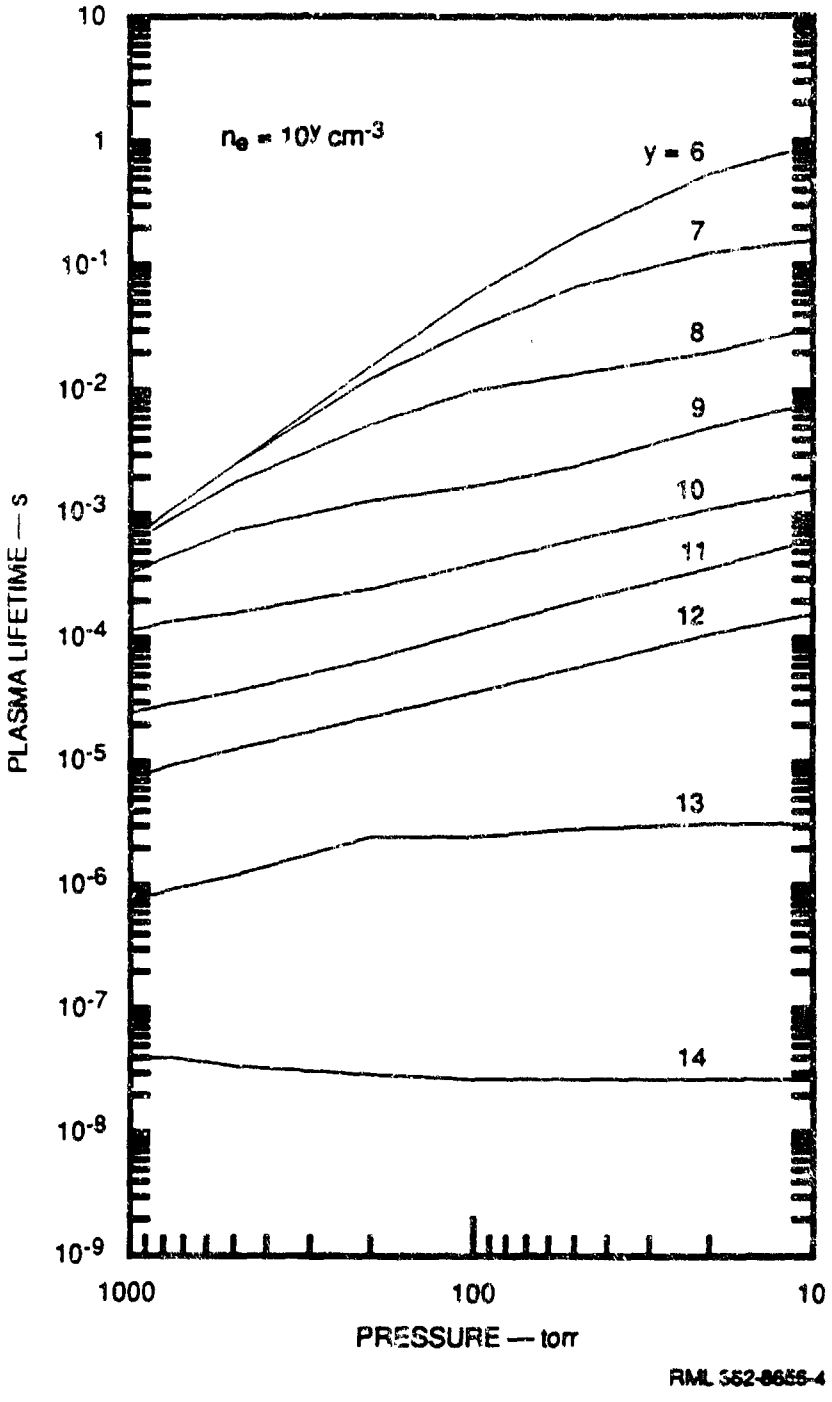

FIGURE 5 PLASMA LIFETIME OF HELIUM WITH 100 ppm AIR

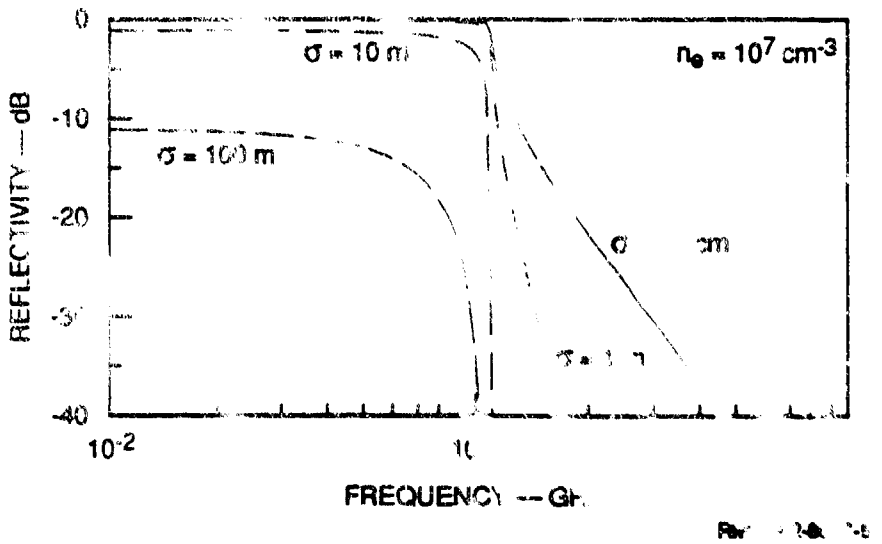

FIGURE 6 REFLECTION FROM AN EPSTEIN PROFILE AT 230 kft (70 km)

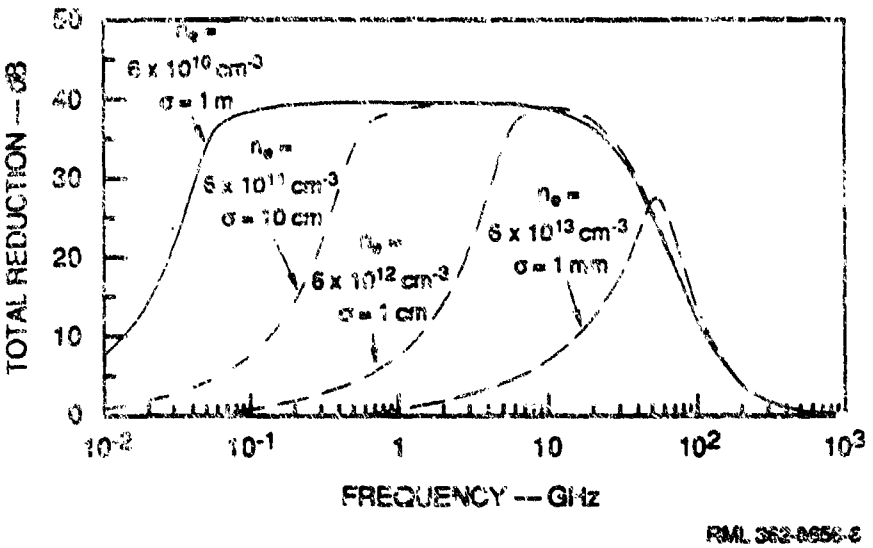

FIGURE 7 ABSORPTION PLUS REFLECTION FROM AN EPSTEIN PROFILE AT SEA LEVEL

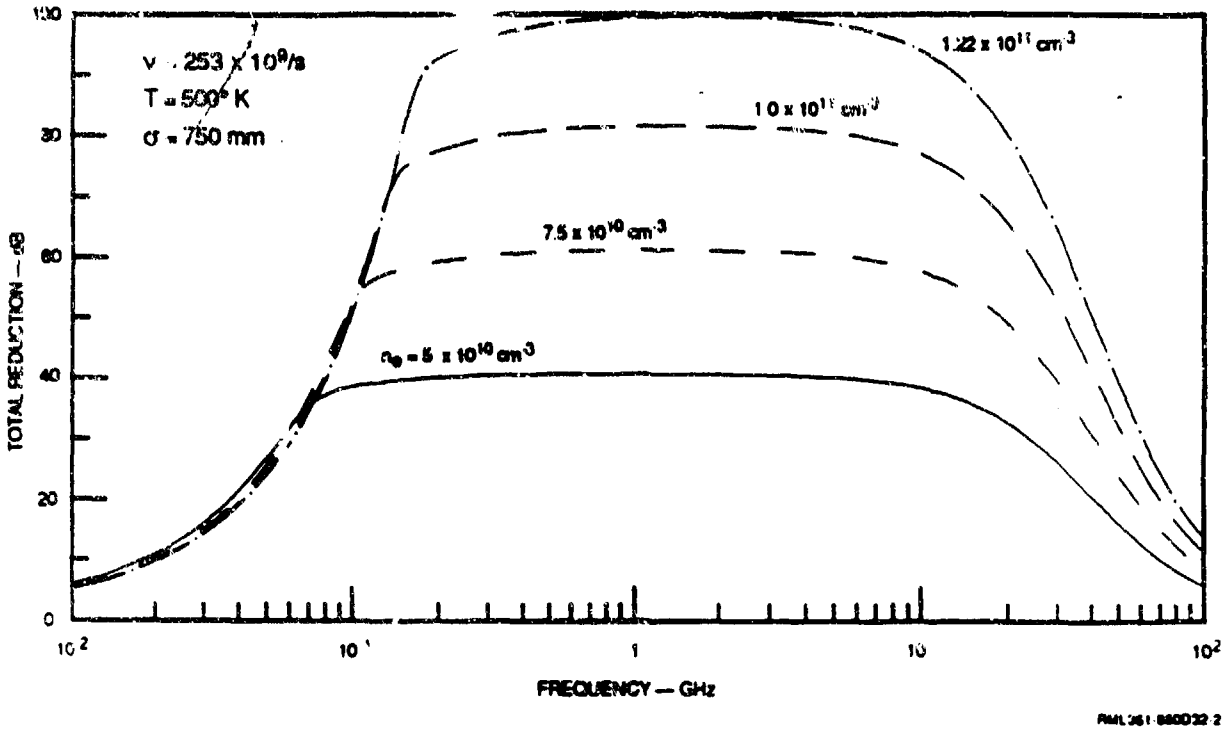

(a) HELIUM

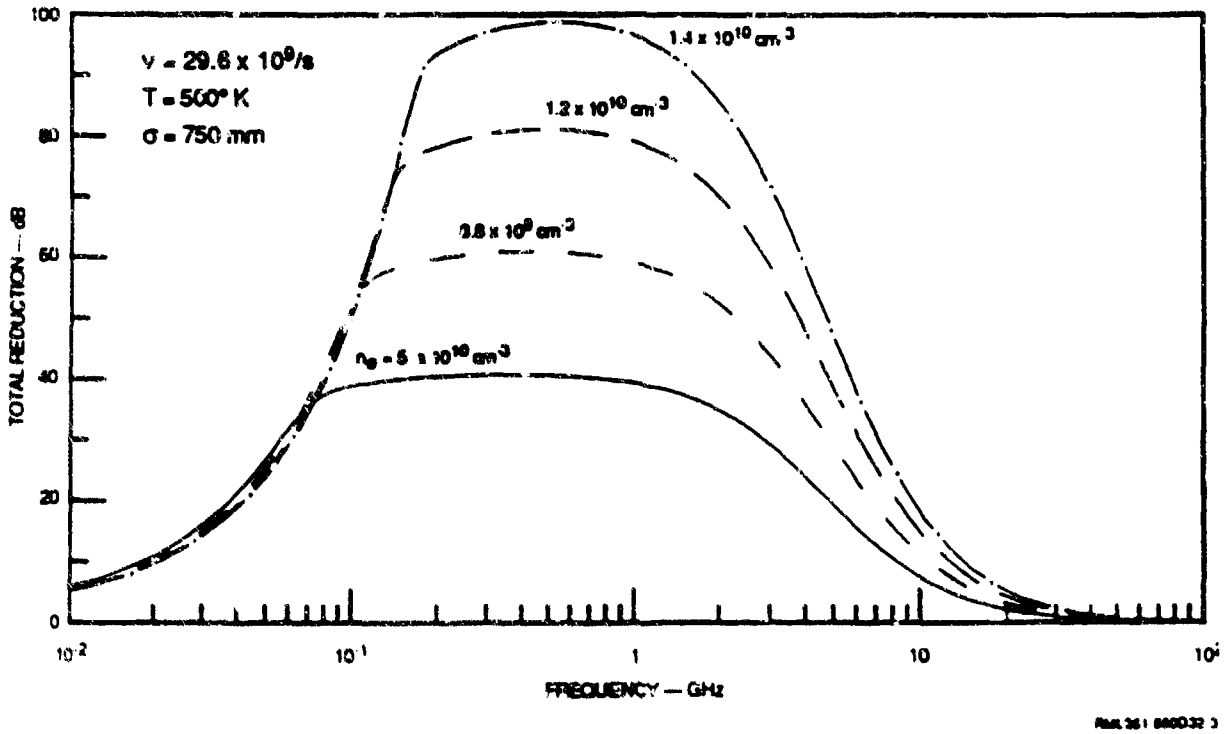

(b) NEON/ARGON

FIGURE 8 ABSORPTION PLUS REFLECTION FROM AN EPSTEIN PROFILE IN HELIUM AND NEON/ARGON AT 760 TORR

ATTACHMENT

REFERENCE 26

D. Watters and R. Vidmar, "Inflatable Target Support for RCS Measurement," AMTA Proceedings, 11th Annual Meeting and Symposium, Monterey, CA, pp. 12–15 to 12–19, 9–13 October, 1989.

AMTA Proceedings, 11th Annual Meeting and Symposium
Monterey, CA, pp. 12-15 to 12-19, 9-13 October 1989.

INFLATABLE TARGET SUPPORT FOR RC. MEASUREMENTS

D. Watters and R. Vidmar

SRI International
333 Ravenswood Avenue
Menlo Park, California 94025

ABSTRACT

A stressed-skin inflatable target support provides an improvement over a foam column for radar cross section (RCS) measurements in an anechoic chamber. Theoretical analysis indicates that backscatter from the support is minimized because its mass is reduced below that of a foam column and is distributed to favor incoherent scattering. Compared with a foam column, a pressurized thin shell has superior mechanical stability under both axial and transverse loads. Experimental observations using Mylar--a low dielectric constant, high tensile strength film--confirm these results. Spurious reflections from rotational machinery located below an inflatable column are reduced by a layer of absorber within the base of the inflatable support.

Keywords: RCS Measurement, Target Support, Stressed Skin, Inflatable Column, Clutter Reduction

1. INTRODUCTION

Anechoic chamber clutter limits both precision and noise floor, making it difficult for RCS engineers to make accurate, low-level RCS measurements. A principal source of clutter is the target support column. A target support column must meet both electromagnetic and mechanical requirements. It must have low RCS over a broad bandwidth and stably support a prescribed weight. For accurate measurement of vector quantities, it is important that the target support be able to return to a reference position after movement.

Traditional target support methods include foam columns, overhead strings, and metal pylons [1]. A foam column has difficulty supporting a heavy load while maintaining a low backscatter, and viscoelastic properties affect its positional accuracy. A string support system is difficult to control and requires an attachment point to the target. Metal ogival pedestals can support heavy loads, but have a larger RCS than other support methods.

An inflatable column offers both low RCS and heavy lift capacity. An inflatable column was designed at RATSCAT in 1964 [2] using nylon-coated neoprene. The column, designed to support 200 lb in a 40-knot wind, was inflated to 0.2 psi and was stable enough to permit vector measurements. Performance of the RATSCAT column was comparable to that of foam. Current advances in material science have given us the ability to fabricate inflatable structures with properties that are superior to foam construction.

An inflatable column has several advantages over a foam column of identical shape. First, an inflatable column has a lower RCS than a foam column. Second, an inflatable column made of a membrane material that is significantly less viscoelastic than foam can have superior mechanical properties, which results in the ability to conduct angular measurements in a more stable manner and to support heavier loads. Finally, ground-related clutter can be reduced over a broad bandwidth by filling the base of the column with broadband absorber.

Section 2 addresses design parameters for an inflatable column, including both electrical and mechanical considerations. Section 3 describes fabrication details that resulted in a prototype structure. Section 4 discusses anechoic chamber measurements, comparing the scattering from a square plate mounted at 45° on a foam column with scattering from the same plate mounted atop the inflatable column.

2. DESIGN CONSIDERATIONS

The two principal requirements for a support column are minimum RCS over a specified frequency range and stable mechanical support up to a specified weight. Design parameters for foam and inflatable columns include: electromagnetic scattering, axial loading, transverse loading, and torsional rigidity. An inflatable column can be designed with minimum RCS and the same or superior mechanical performance compared with a foam column.

2.1. Electromagnetic Properties

The electromagnetic scattering from a column can be estimated by considering the two-dimensional scattering from a class of infinite cylinders [3]. A model for scattering from a foam column is a solid dielectric cylinder whose permittivity is nearly unity. The scattering cross section per unit length is:

$$\frac{\sigma_1}{\pi a} = \frac{\sigma_1}{\pi a} = \frac{\pi}{4}k_0 a(\epsilon_r - 1)^2 J_1^2(2k_0 a)$$

where a is the radius of the cylinder, k_0 is the free space wave number, and ϵ_r is the relative permittivity of the cylinder. The response is the same for either parallel or perpendicular polarization.

For an inflatable column, similar expressions can be derived, where the model is now a cylindrical shell. The scattering cross section per unit length is:

$$\frac{\sigma_1}{\pi a} = \pi(k_0 a)^3(\epsilon_r - 1)^2\left(\frac{d}{a}\right)^2 \cdot \left|\sum_{n=0}^{\infty} \epsilon_n(-1)^n J_n^2(k_0 a)\right|^2$$

$$\frac{\sigma_1}{\pi a} = \pi(k_0 a)^3(\epsilon_r - 1)^2\left(\frac{d}{a}\right)^2 \cdot \left|\sum_{n=0}^{\infty} \epsilon_n(-1)^n\left[J_n'^2(k_0 a) + \frac{n^2}{k_0^2 \epsilon_r a^2} J_n^2(k_0 a)\right]\right|^2$$

where $\epsilon_n = 1$ when $n = 0$ and $\epsilon_n = 2$ when $n > 0$, and d is the shell thickness. Slightly different values are obtained for parallel and perpendicular polarization.

Figure 1 is a plot of scattering per unit length as a function of frequency for a 12-in. diameter foam cylinder of permittivity 1.04 (dashed curve) and a 12-in. diameter Mylar shell of thickness 0.002 in. and permittivity 2.8 (solid curve). At low frequencies, scattering from the inflatable structure is considerably reduced compared with that from a foam column. At sufficiently high frequencies, this inflatable column would exhibit a high RCS because the film thickness approaches a significant fraction of a wavelength.

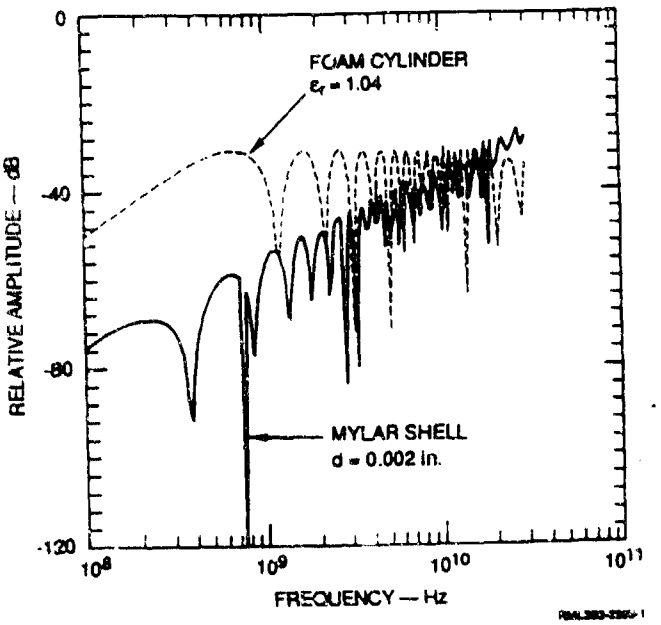

Fig. 1. Normalized Backscatter Cross Section per Unit Length from Infinitely Long Cylinders

Cone-shaping of either column can be used to further reduce the direct backscatter.

2.2 Mechanical Properties

The model for comparison of mechanical properties is a column that is fixed at one end and free to move at the other. The maximum buckling load, W, for a foam column is given by [4]:

$$W = \frac{\pi^3 a^4 E}{16L^2}$$

where a is the radius of the column, L is the height, and E is the elastic modulus. The maximum load for an inflatable column is determined by the cross-sectional area at the top and the pressure in the column.

The pressure, P, in the column is limited by the maximum hoop stress, S = Pa/d, (which occurs at maximum radius). The maximum load is: W = πadS, where d is the film thickness. For taller columns, it is appropriate to consider failure due to buckling:

$$W = \frac{\pi^3 a^3 dE}{4L^2}$$

A 10-ft foam column of 6-in. radius and elastic modulus of 1000 psi is capable of supporting 43 lbs, with a safety factor of 4. A 10-ft air column of 6-in. radius would need to be inflated to 0.75 psi to support a similar load. For a cylindrical column, this pressure would exert a 4.5 lb/in. hoop stress (Sd) at the base. A safety factor of two would require the cylinder to withstand 9 lb/in. For a conical column with a base radius of 16 in., the stress at the base would require a design of 12 lb/in. This can be accomplished using 2-mil Mylar. (For comparison, about 20 mils of polyethylene film would be needed to meet the same stress requirement.)

The deflection of a column under transverse loading can be determined to first order using small deflection theory. For a conical foam column, the maximum deflection is:

$$y_{max} = \frac{4FL^3}{3EI_c\left(1 + \frac{\Delta r}{r_1}\right)}$$

where $\Delta r = r_2 - r_1$, r_1 is the radius at the top, r_2 is the radius at the base, $I_c = \pi r^4/4$ for a solid circle, and F is the transverse force.

For an inflatable column, the deflection is:

$$y_{max} = \frac{FL^3}{EI_a}\left[\left(\frac{r_1}{\Delta r}\right)^3 \ln\left(1 + \frac{\Delta r}{r_1}\right) - \left(\frac{r_1}{\Delta r}\right)^2\left(\frac{1 + \frac{3\Delta r}{2r_1}}{\left(1 + \frac{\Delta r}{r_1}\right)^2}\right)\right]$$

where $I_a = \pi r^3 d$ for a thin annulus.

A comparison of a foam and inflatable construction using the above dimensions indicates that a 10-lb transverse load applied to a 97-in. column will produce a 0.112-in. deflection of a foam column and a 0.332-in. deflection of an inflatable column. (The elastic modulus of Mylar is 500,000 psi)

Although the foam and inflatable columns exhibit similar characteristics, foam is much more viscoelastic than Mylar. Consequently, a full comparison between foam and inflatable construction must treat how the elastic modulus varies as a function of time, temperature, and stress. For example, the elastic modulus may decrease by a factor of 10 in 1 hour while a high stress is applied. This variation in E with time results in a time-dependent deflection. Foam may exhibit an additional deflection of 10%, while Mylar creep is an order of magnitude less. Under severe loading, a foam column may never return to its reference position after the transverse load is removed.

The response of a cylindrical column under torsion can be analyzed using the following equation [5]:

$$\theta = \frac{TL(1 + \nu)}{EI}$$

where θ is the angular displacement, T is the applied torque, I is the moment of inertia for a body of revolution (I_c and I_a), and ν is Poisson's ratio. A comparison of the two columns indicates that the foam column exhibits an angular displacement of 0.0016°/ft-lb; while the inflatable column changes 0.0024°/ft-lb.

Although the deflections and angular displacements of this version of the inflatable column are slightly higher than those of a foam column, the inflatable returns to its reference position, reliably. The reliability of return opens up the possibility of high accuracy measurements involving vector subtraction.

3. CONSTRUCTION

The cone-shaped column in Figure 2 was constructed using 2-mil Mylar film. The column is inflated to 0.75 psi, using nitrogen gas, and can support a load of 50 lb. The vertical bag seams are double lap joints using an adhesive tape on both the inside and outside. Stress testing indicates that the material will fail before the adhesive joint. A heat-shrinkable film is applied to a foam plug and inserted at the top of the column. The internal pressure of the bag forces the tapered foam plug to seal the top of the bag. The base is constructed using an aluminum-foam sandwich, with the foam cantilevered beyond the aluminum plates. This arrangement permits absorber, placed inside the column, to cover the aluminum plate. A ring of flat laminate absorber is placed around the outside of the column to complete the RF seal to the base. The Mylar bag is attached to the base using a special adhesive technique.

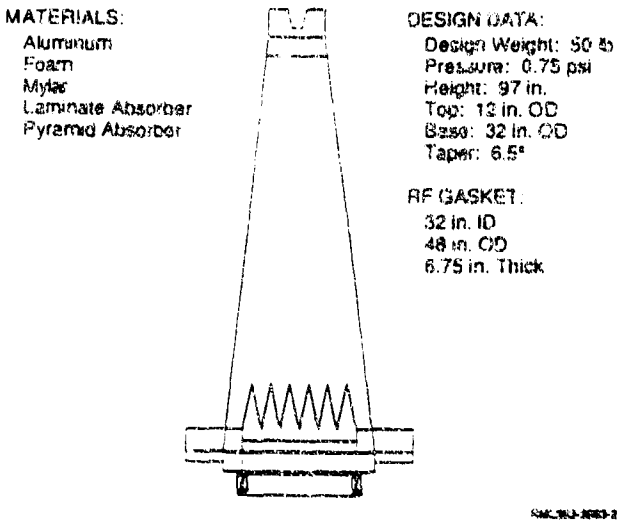

Fig. 2. Stressed-Skin Inflatable Structure

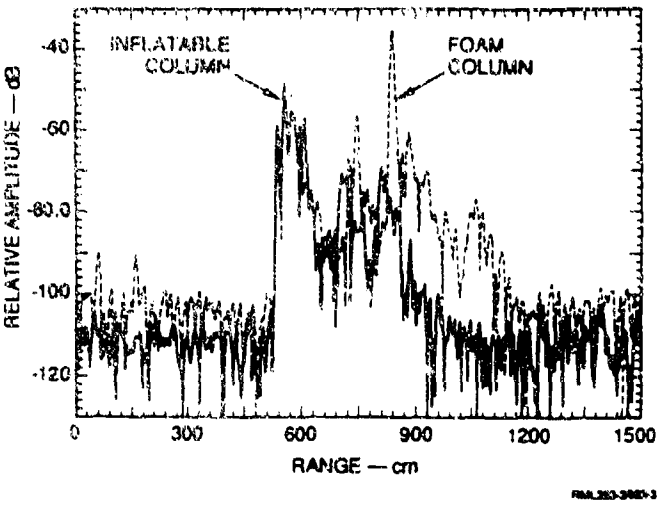

Fig. 3. Scattering From a 45° Plate

Two prototype columns have been constructed and inflated to the design pressure of 0.75 psi. They have operated reliably for three months and are continuing to operate at the time of this submission. Design lifetime is one year or more.

4. PERFORMANCE

Preliminary measurements on the cone-shaped inflatable column have been made in our anechoic chamber [6] using an HP-8510 automatic network analyzer. A comparison is made between the foam column and the inflatable column.

A 45° plate, 14 in. on a side is mounted on the column, in a way to cast a direct reflection toward the base. Figure 3 is a range domain plot of the foam column and inflatable column responses. The horizontal axis represents range in centimeters, the vertical axis is relative amplitude in dB, and the frequency of operation is 600-4600 MHz. The measurement was made using the bare column as a reference and then subtracting this reference from the measurement obtained with the plate on top of the column.

Both curves display three main scattering peaks. Proceeding downrange from the illuminating horns, the first peak represents the scattering from the plate. The fine structure is scattering from the tip, corners, and tail. Small differences between the two curves is attributed to placement of the 45° plate.

The second peak is a triangular path representing scattering from the plate to the base of the column and back to the horn (or vice versa.) The response occurs earlier in time for the inflatable column because its base is higher than the base of the foam column. The amplitude of the response for the inflatable column is reduced by 20 dB over the foam column measurement. This reduction is due to the absorber in the base of the air column.

The third peak is determined by scattering from the plate to the base of the column, back to the plate, and then returning to the receive horn. For the foam column, this double bounce path is the dominant scatterer. For the inflatable column, the double-bounce response occurs earlier in time and is 35 dB below the foam column result. Additional attenuation of this double bounce can be obtained by using better (taller) absorber.

Looking further downrange, multiple reflections from the base of the foam column persist for some time. This is not apparent when the inflatable column is used, resulting in a reduction of about 10 dB in ground-related clutter.

Although an inflatable column offers a means to reduce scatter from its base, backscatter from the top plug dominates backscatter from the column. Because the foam density and dielectric constant of the plug of the inflatable column are similar to those of a good quality foam column, backscatter per unit length from the plug is the same as that from a foam column.

Total backscatter from the inflatable column may be significantly less than or equal to backscatter from a foam column, depending on how much of the column is illuminated. If all of the inflatable column is illuminated, backscatter from the plug will dominate scatter from the Mylar skin. However, the length of the plug is typically less than 10% of the total length of a foam column. Hence, backscatter from a completely illuminated inflatable column would be at least 10 dB less than that from a foam column.

At some facilities only a portion of the support column is illuminated. For example, the preliminary measurements reported in this paper were obtained in an anechoic chamber with high-gain horns pointed toward a spot 2 ft above the support column. Test bodies are elevated to this spot with foam fixtures that mount to the support column. Backscatter was primarily from the test body, its foam mount, and foam from the top of the support column. Because of this mounting arrangement, the amount of foam illuminated is nearly the same for the inflatable and foam columns. Measured backscatter from the two columns was roughly equal. An improved version of the inflatable column described above would include a plug contrived to minimize backscatter without compromising structural integrity.

Because the top plug is the major source of backscatter, it is the current focus of research. Techniques to reduce its backscatter are under consideration and several candidate designs have been developed. A second area of interest is development of an inflatable support of greater load rating which is optimized for transverse and torsional rigidity.

5. SUMMARY

An inflatable support has been constructed and tested. Because this support is hollow, the inside of its base can be covered with broadband absorber to reduce reflections. Use of foam has been minimized to a short plug at the top of the column. This plug is the dominant source of backscatter. An inflatable support has attractive mechanical features. Because the plug is short compared to the length of the inflatable column, the transverse and torsional rigidity of the column is based on the mechanical properties of a pressurized thin-shell Mylar cone. Mylar is much less viscoelastic than typical foams, so variations in elastic modulus with time, temperature, and applied load are less for Mylar. Because transverse and torsional deflections are inversely proportional to the elastic modulus, the reference position of an inflatable column is better defined and can be recovered after transverse or torsional deflections. These electrical and mechanical benefits suggest that inflatable supports are beneficial to high-accuracy vector measurements.

6. ACKNOWLEDGMENTS

Initial work has been supported by Independent Research and Development funds at SRI International. An invention disclosure is in process. The authors acknowledge Gerry Andeen for his assistance in mechanical design.

7. REFERENCES

1. H.L. Wolfenbarger and P.E. Amador, "Electromagnetic and Structural Considerations in Target Support Design," AMTA Proceedings, 10th Annual Meeting and Symposium, p. 8-3, September 1988.

2. Radar Cross-Section Target Supports--Plastic Materials, RADC Center, No. TDR-64-381, AD608252, June 1964.

3. G.T. Ruck, et al., Radar Cross Section Handbook, Plenum Press, 1970, pp. 205-263.

4. C.C. Freeny, "Target Support Parameters Associated with Radar Reflectivity Measurements," Proc. IEEE, Vol. 53 p. 929, 1965.

5. W.C. Young, Roark's Formulas for Stress and Strain, 6th Ed., McGraw Hill, 1989.

6. D.G. Falconer, "Extrapolation of Near-Field RCS Measurements to the Far Zone," IEEE AP-36, no. 6, p. 822-835, June 1988.